On the prediction of the bi-axial failure envelope of a UD CFRP composite lamina using computational micromechanics: *effect of microscale parameters on macroscale stress-strain behavior*

A. Sharma [a], S. Daggumati[b*], A. Gupta[a], W. Van Paepegem[c]

[a]Discipline of Mechanical Engineering, Indian Institute of Technology Indore, Simrol, Indore 453552, India

[b]Department of Mechanical Engineering, Indian Institute of Technology Tirupati, Tirupati, A.P. 517506, India

[c]Department of Materials, Textiles and Chemical Engineering, Ghent University, Technologiepark–Zwijnaarde 46, B-9502 Zwijnaarde, Belgium

ABSTRACT

A computational micromechanics based Finite Element (FE) analysis methodology is presented to predict the bi-axial failure envelope of a unidirectional (UD) carbon-epoxy composite ply. In order to estimate the effect of various microscale parameters that are influencing the macroscopic stress-strain behavior, under individual load cases, detailed numerical studies are conducted using a 3D RVE (Representative Volume Element) model. The constituent epoxy matrix plastic deformation in the RVE is captured using the linear Drucker-Prager plasticity model.

---

*Corresponding author. Tel.: +91. 8008890 497;
E-mail: subbareddy.daggumati@iittp.ac.in

The effect of the fiber-matrix interface damage, followed by frictional sliding of the constituent materials on the computed interface tractions is captured using a cohesive zone damage model combined with the Coulomb friction law, which is implemented into Abaqus using VUMAT. From the detailed FE analysis of the RVE under individual load cases, it is observed that the predicted macroscopic stress-strain behavior is sensitive to the fiber-matrix interface properties as well as the in-situ epoxy stress-strain behavior. Hence, using a coupled experimental-computational micromechanics approach the interface and the in-situ epoxy material properties are calibrated and validated. Using the calibrated interface and in-situ epoxy material properties, the bi-axial (transverse tension / transverse compression – in-plane shear) failure envelope of a UD composite ply is estimated. Comparing the predicted damage profiles and the failure envelope with the experimental results leads to good agreement and validates the proposed numerical methodology.

Keywords: Polymer Matrix Composites (PMCs); plastic deformation; computational micromechanics; interface damage, bi-axial failure envelope.

1. Introduction

Attributed to the excellent specific strength and stiffness Polymer Matrix Composites (PMCs) find extensive structural applications in advanced mechanical industries such as energy, aviation, and aerospace.

Unlike other structural materials, PMCs are hierarchical with three distinct length scales namely, microscale, mesoscale and macro-scale. Pertaining to each length scale, there exist specific damage initiation and propagation mechanisms.

In general, composite structures are designed to undergo multi-axial load conditions during their service life. Hence, over the years numerous ply/laminate level failure models have been proposed to predict the multi-axial failure envelope. The aforementioned failure criteria can be broadly categorized into stress based [1] [2] [3] [4], strain based [5] [6], and phenomenological models [7] [8] [9] [10]. In order to evaluate the robustness of the state-of-art failure theories related to PMCs, Soden et al. [11] [12] [13] conducted the 'World Wide Failure Exercise (WWFE)'. Consequently, various failure theories were ranked according to their predictive capabilities. However, at the end of the abovementioned failure exercise, the general consensus was that there is a discrepancy between predicted and experimental failure envelopes [9] [14]. Since then many efforts have been devoted for developing generalized failure criteria for PMCs through the incorporation of specific failure modes (e.g. Puck et al. [7]), which can effectively predict the bi-axial failure envelopes of FRP laminates [4] [8] [15] [16].

The mechanical properties of fiber-reinforced composites depend on the fiber, matrix, fiber distribution, orientation, and void content. Besides the aforementioned properties, at the micro-scale, the nature of the fiber-matrix interfacial bonds and the mechanisms of load transfer between different constituent materials play an important role [17].

Attributed to the above mentioned complex microstructural parameters, phenomenological or macro-scale damage models cannot accurately describe the complex failure behavior of Fiber Reinforced Polymer (FRP) composites [18]. For the aforesaid purpose, computational micromechanics present the following distinct advantages: a) the influence of the geometry and the spatial distribution of the fibers can be accurately taken into account; b) the obtained detailed stress-strain fields throughout the microstructure can lead to precise estimates of the onset and propagation of damage, and accurate predictions of the failure and strength [19]. Consequently, developing a thoroughly validated micromechanics based failure criterion with physical soundness is a clear advance over the state-of-art phenomenological damage models. Hence, with the ultimate goal of predicting the failure envelope of a UD composite ply under multiaxial loads, Gonzalez et al. [20]–[24] presented a detailed computational micromechanical procedure for UD FRP composite plies. The general micromechanical modeling strategy of the above mentioned studies consists of the following steps: i) an RVE model is generated using the Random Sequential Adsorption (RSA) algorithm for creating a random fiber distribution that mimics the fiber placement observed in an actual composite ply; ii) the fiber-matrix interface damage is modeled with a bi-linear traction separation law; iii) to account for the matrix yield behavior, either Mohr-Coulomb or Drucker-Prager plasticity model was used. Using a similar approach, Vaughan et al. [25] conducted the micromechanical studies under transverse tensile load on a UD carbon-epoxy composite ply. In the aforesaid study [25], the Nearest Neighbor Algorithm (NNA) was used to generate an RVE model with random fiber distributions.

The above mentioned research work has shown the effect of RVE size, matrix plasticity model and various fiber/matrix interface parameters on the predicted stress-strain and damage behavior of the UD FRP composite plies.

Even though several researchers tried to predict the ply level stress-strain behavior and the bi-axial failure envelopes of a UD composite ply using computational micromechanics, often these results are not directly compared (one-on-one) with the experimental results. This can be attributed to the fact that there is a lack of reliable fiber/matrix interface data in the open literature. Moreover, related to the matrix material behavior, as stated by Fiedler et al. [26] *the polymer matrix behaves differently in a composite ply compared to its bulk form. In addition, a detailed study is missing regarding the influence of in-situ epoxy material properties on the predicted RVE average stress-strain behavior.*

In general, for the micromechanical FE simulations, the bulk epoxy material properties are used [19][22][25][27]. However, as stated by Hobbiebrunken et al. [28], *"the strength and the capability of plastic deformation of the epoxy matrix is controlled by the matrix physics properties as well as by the acting stress state and stressed volume"*. In this regard, from the microscale tension testing of thin epoxy circular rods (ø=36.7 µm) [28] to nano-indentation tests accomplished on the in-situ epoxy [21][29][30] reveal that the tension and compression strength values obtained from the bulk epoxy testing are approximately 20-55% lower than the strength values obtained from in-situ (nanoindentation) and microscale epoxy tests.

Similar to the aforementioned observations, based on the microcompression tests conducted using epoxy micropillars, Wang et al. [31] concluded that there is a significant size effect on the measured yield strength, and exhibiting the relation of "the smaller, the harder". The enhanced Young's modulus and yield strength of the epoxy matrix under microscale tension and compression tests is attributed to the diminishing number of available weak bonds.

Considering the goal of the current numerical study i.e. estimating the bi-axial failure envelope of a UD composite ply, while understanding the influence of microscale parameters on the macroscopic stress-strain behavior, the following numerical methodology is employed. i) an RVE model is generated using the fibers distribution and the placement of the fibers observed in a microscopic image of an actual UD composite ply; ii) initially, Abaqus built-in cohesive zone module is used to capture the fiber/matrix interface damage initiation and propagation. However, under the applied transverse compression load, to facilitate the load carrying capability of the fiber and matrix surfaces after the interface element damage, friction combined with a cohesive damage model [32] is implemented into Abaqus/explicit using VUMAT. iii) in order to model the effect of hydrostatic stresses on the yield behavior of the epoxy matrix, the linear Drucker-Prager plasticity model combined with the nondilatant flow rule is employed; iv) under the applied individual load cases, a coupled experimental-computational study is conducted to calibrate and estimate the influence of various microscale parameters such as interface strength, fracture energy, friction and in-situ epoxy stress-strain behavior on the predicted RVE average stress-strain response;

vi) finally, the proposed numerical methodology is extended to predict the bi-axial failure envelope, and the obtained numerical strength values are compared to the experimental failure envelope [33]. Here, the authors want to highlight that, in the current research work the effect of the random distribution of the interface properties on the predicted macroscopic stress-strain behavior is not considered. For more information on this aspect, readers are referred to the research work of Naderi et al. [34]. Moreover, the effect of the voids, as well as thermal residual stresses are also not considered as a part of the current computational work.

2. Computational micro-mechanical modeling methodology

2.1. RVE FE model

In order to accomplish the micromechanical FE analysis, an RVE model with random fiber distribution needs to be created. The chosen fiber placement in the RVE must be statistically representative of the fiber distribution that is observed in an actual composite ply. Also, the chosen RVE should be large enough so that the average properties of this volume element are independent of its size and position within the material [24]. Regarding the optimal size of an RVE that needs to be used for computational micromechanical analysis, Naya et al. [21] concluded that an RVE model having approximately 50 fibers can adequately capture the essential features of the composite microstructure. Hence, for the current numerical studies, a 49 fibers RVE model is generated. In addition, the created RVE model is based on the fiber placement observed in an actual microscopic image of a UD composite ply [35]. As highlighted in Fig 1a, a section of a composite ply is selected in such a way that the local fiber volume fraction in the chosen field of view is similar to the macroscopic fiber volume fraction (60%) of the composite.

As shown in Fig 1b, the obtained non-periodic fiber distribution is converted into a periodic microstructure using the following procedure. The fibers highlighted in red circles (Fig 1b) belong to the periodic microstructure. However, the edge fibers marked by the blue circles (B1, B2, and T1) hinder the periodicity of the microstructure. Hence, to facilitate the periodicity, corresponding to B1, B2 and T1 fibers, B1', B2' and T1' are created on the opposite face of the RVE (Fig 1b). Finally, the fiber marked by the yellow circle is removed from the selected field of view. Consequently, the generated RVE CAD model (Fig 1c) is a perfectly periodic microstructure. Here it should be emphasized that the above mentioned RVE CAD model generation process is completely automated with the help of a python script. For the aforesaid python program, the input data need to be provided in the form of individual fiber centroids as well as the fiber diameter.

As shown in Fig 1d, the generated RVE model has a square shape with an equal length and width of 53.4 µm, and a thickness of 1.65 µm. From the RVE thickness point of view, previous studies of Totry et al. [36] concluded that the chosen RVE thickness does not show any influence on the predicted numerical results. Hence, the chosen RVE thickness (1.65 µm) for the current numerical simulations is a compromise between the aspect ratio of the FE mesh to the speed of the numerical simulations. Moreover, since the crack tunneling is not considered in the current modeling work, choosing a small thickness (1.65 µm) of the RVE is justifiable [37].

In order to accomplish the micromechanical simulations, the RVE geometrical model is translated into an FE mesh using continuum 3D elements in Abaqus. The FE mesh of the RVE model (Fig 1d) consists of a majority of C3D8R elements along with few C3D6R elements. The generated RVE model consists of IM7 carbon fiber as reinforcement and the epoxy matrix (Hexcel 8552) as a binder material. For the RVE modeling purpose, the carbon fiber diameter is taken as 6.6 μm [25] and the overall fiber volume fraction of the RVE is maintained at 60%.

From the RVE boundary conditions perspective, to capture the periodicity of the stress-strain fields, the periodic boundary conditions (PBCs) are imposed on the RVE model as specified in [38]. In order to apply the PBCs, initially, a conformal FE mesh is generated for the above mentioned RVE model (Fig 1c). Moreover, the application of PBCs to the RVE model is automated with the help of a MATLAB script. Finally, the fibers in the RVE do not contribute to the transverse damage, hence, the fibers are considered as elastic and transversely isotropic materials (Table 1). Consequently, the following sections present a detailed description of the material models used for the interface and the epoxy matrix.

2.2. Fiber-matrix interface damage modeling

For simulating the damage initiation and subsequent damage propagation of the interface, three dimensional eight noded cohesive elements (COH3D8) having a thickness of 0.1 μm were inserted between the fiber and matrix in the RVE (Fig 1d).

The constitutive response of these elements is governed by the bi-linear traction-separation law [38], which relates the separation across the interface with the traction vector acting upon it. In general, the cohesive elements damage initiation is modeled using either maximum nominal stress or quadratic stress criteria. The damage propagation is modeled using mixed mode fracture criteria [39] [25] [22] [24]. After the interface element final failure, its load resisting capability is reduced to zero. However, for an RVE under transverse compression, the friction between fiber-matrix surfaces must offer some resistance to the applied external load even after the complete failure of the interface element [32]. In this regard, to incorporate the effect of friction on the interface tractions, Alfano et al. [40] proposed a mixed mode damage evolution criteria combined with the Coulomb friction law. In similar guidelines, Van Der Meer et al. [41] and Chevalier et al. [42] used the CZM coupled with Coulomb friction law.

For the current numerical studies, a cohesive zone model that consists of interface damage combined with the Coulomb friction law is implemented into Abaqus/explicit using VUMAT as proposed by [40] [41] [42] [43]. In the current section, firstly, detailed formulations of the implemented cohesive zone damage model into Abaqus will be explained. Later, the conjunction of the frictional effects with the cohesive zone damage model will be discussed. The constitutive equation for the linear elastic behavior of the aforesaid traction separation law is defined through the following equation.

$$\begin{bmatrix} t_1 \\ t_2 \\ t_n \end{bmatrix} = \begin{bmatrix} K_1 & 0 & 0 \\ 0 & K_2 & 0 \\ 0 & 0 & K_n \end{bmatrix} \begin{bmatrix} \delta_1 \\ \delta_2 \\ \delta_n \end{bmatrix} \quad (1)$$

In the above equation t_n, t_1, and t_2 are the normal (Mode I) and shear (Mode II & Mode III) stresses at the interface, while the corresponding displacements are denoted by δ_n, δ_1, and δ_2 respectively. Besides, K_n, K_1, and K_2 are the values of interface stiffness corresponding to Mode I, Mode II and Mode III respectively. Here, it should be mentioned that for the current numerical studies the values of normal and shear stiffness are assumed to be equal (i.e. $K_n=K_1=K_2=K$). The interface damage is assumed to be governed by the effective mixed mode displacement λ which is defined by the following expression [43].

$$\lambda = \frac{K_1\delta_1^2+K_2\delta_2^2+K_n\langle\delta_n\rangle^2}{\sqrt{K_1\delta_1^2+K_2\delta_2^2+K_n\langle\delta_n\rangle^2}} \quad (2)$$

For interface damage initiation, the damage activation function $F(\lambda)$ is defined as follows [43].

$$F(\lambda) = H(\lambda) - \rho_d \leq 0 \quad (3)$$

As soon as the above mentioned damage activation function reaches zero, the interface damage will be initiated. In the above equation ρ_d is a threshold function, and $H(\lambda)$ is a function of effective displacement which evolves monotonically after damage initiation. These functions are updated at every time step 't' during the numerical analysis, which are defined as follows:

$$H(\lambda) = \min\{\frac{(\lambda-\lambda^0)}{(\lambda^f-\lambda^0)}, 1\} \quad (4)$$

$$\rho_d = \max\{0, max_s\, H(\lambda)\}\ 0 < s < t \qquad \forall t \quad (5)$$

In Eqn 4, λ^0 and λ^f are the effective mixed mode displacement jumps corresponding to damage initiation and final failure of the interface respectively (Fig 2b). Whereas λ is the instantaneous effective displacement computed at every time step during the analysis. Using the quadratic nominal stress criterion [44] in combination with the individual traction separation equations, λ^0 is calculated using the following equation [45].

$$\lambda^0 = \begin{cases} \delta_n^0 \delta_1^0 \sqrt{\frac{1+\alpha^2}{(\delta_2^0)^2+(\alpha\delta_n^0)^2}}, & \delta_n > 0 \\ \sqrt{(\delta_1^0)^2 + (\delta_2^0)^2}, & \delta_n \leq 0 \end{cases} \tag{6}$$

Where, α = mode-mixity ratio = $\frac{\sqrt{(\delta_1)^2+(\delta_2)^2}}{\delta_n}$

In addition, λ^f is calculated using the Benzeggagh-Kenane (BK) mixed-mode fracture criteria [46] and is given in the following form.

$$\lambda^f = \begin{cases} \frac{2}{K\lambda^0}\left[G_n^c + (G_s^c - G_n^c)\left(\frac{\alpha^2}{1+\alpha^2}\right)^\eta\right], & \delta_n > 0 \\ \sqrt{(\delta_1^f)^2 + (\delta_2^f)^2}, & \delta_n \leq 0 \end{cases} \tag{7}$$

In the above equation, G_n^c is the critical normal fracture energy and G_s^c is the critical shear fracture energy. Moreover, η represents the BK power-law coefficient and is taken as 1.45 [27]. Finally, the constitutive equation for mixed-mode interface failure for the cohesive zone damage model without frictional stresses is defined by the following expression.

$$\tau = \begin{cases} \tau^u & ; \lambda \leq \lambda^0 \\ (1-D)K\delta_i, i = n, 1, 2 & ; \lambda > \lambda^0 \end{cases} \tag{8}$$

In the above equation, τ^u represents the undamaged part of the interface stresses. Whereas 'D' is a scalar damage variable, which evolves monotonically from zero (no damage) to one (complete damage) and is defined as follows [43]:

$$D = \frac{\rho_d \lambda^f}{\rho_d \lambda^f + (1-\rho_d)\lambda^0} \quad (9)$$

The above described set of equations (1-9) can fully estimate the damage initiation and evolution at the fiber-matrix interface under mixed mode load conditions. However, under specific load cases such as transverse compression, to capture the effect of friction between the fiber and matrix surfaces on the interface stresses, the above discussed cohesive zone model should be combined with a proper friction law. According to Alfano et al. [40], the interface tractions corresponding to a Representative Elementary Area (REA) (Fig 2a) can be divided into a damaged (τ_d) and an undamaged part (τ_u). Also, the relative displacements corresponding to both the parts across the REA are assumed to be equal and constant ($\delta^u = \delta^d = \delta$) [40] [42]. The homogenized interface traction over the entire REA can be described in the following expression.

$$\tau = (1 - D)\tau^u + D\tau^d \quad (10)$$

In the above equation the first term $[(1 - D)\tau^u]$ defines the cohesive damage law, while $D\tau^d$denotes frictional stresses on the damaged interface. Similar to the assumption of REA interface stresses, the displacements corresponding to the damaged part of the REA is divided into an elastic (δ^{de}) and inelastic (δ^{di}) part (Eqn 11), with δ^{di} corresponding to the frictional sliding.

$$\delta^d = \delta^{de} + \delta^{di} \quad (11)$$

The following constitutive equation relates the displacements ($\delta^{de} = \delta - \delta^{di}$) to corresponding tractions (τ^d) during the softening phase (Fig 2b).

$$\tau^d = \begin{bmatrix} K_1 & 0 & 0 \\ 0 & K_2 & 0 \\ 0 & 0 & K_n \end{bmatrix} \begin{bmatrix} \delta_1 - \delta_1^{di} \\ \delta_2 - \delta_2^{di} \\ -\langle -\delta_n \rangle \end{bmatrix} \tag{12}$$

Here, it should be noted that the utilization of the Macaulay bracket in the above equation implies that compressive normal displacement does not affect the interface damage model. In the above equation, δ_1^{di} and δ_2^{di} represent the inelastic sliding occurring due to friction (Fig 2b) in the damaged part of the REA. The evolution of inelastic frictional sliding is governed by the following equation [42]:

$$\delta^{di} = \lambda \begin{bmatrix} \frac{\partial \phi}{\partial \tau_1^d} \\ \frac{\partial \phi}{\partial \tau_2^d} \\ 0 \end{bmatrix} \tag{13}$$

In Eqn 13 'ϕ' is a friction function and λ corresponds to the displacement jump defined previously by Eqn 2. The friction function ϕ is defined as follows:

$$\phi = \mu \tau_n^d + \tau_s^d. \tag{14}$$

Where, $\tau_s^d = \sqrt{\left(\tau_1^d\right)^2 + \left(\tau_2^d\right)^2}$

Finally, the constitutive equation for the interface damage combined with the Coulomb friction law takes the following form:

$$\tau = (1 - D) \begin{bmatrix} K_1 & 0 & 0 \\ 0 & K_2 & 0 \\ 0 & 0 & K_n \end{bmatrix} \begin{bmatrix} \delta_1 \\ \delta_2 \\ \delta_n \end{bmatrix} + D \begin{bmatrix} K_1 & 0 & 0 \\ 0 & K_2 & 0 \\ 0 & 0 & K_n \end{bmatrix} \begin{bmatrix} \delta_1 - \delta_1^{di} \\ \delta_2 - \delta_2^{di} \\ -\langle -\delta_n \rangle \end{bmatrix} \tag{15}$$

Summarizing the above described damage methodology, Fig 2c shows a detailed flow-chart of the implemented interface damage model combined with the Coulomb frictional law. In order to validate the implemented VUMAT code, the predicted numerical stress-strain curves without frictional effects are compared to the stress-strain curves obtained using Abaqus built-in cohesive zone model.

2.3. Epoxy material modeling

It is a well documented fact that the yield behavior of the polymeric materials is sensitive to the hydrostatic pressure. As a consequence, the yield stress in tension becomes different from the yield stress in compression [47]. In this regard, the mechanical behavior of polymer material can be appropriately modeled by using the Drucker-Prager plasticity model [6], which incorporates a linear dependence on hydrostatic stress. The following equation describes the yield criterion for the linear Drucker-Prager model.

$$F = t - p\tan\beta - d = 0;\ t = \frac{1}{2}\, q \left[\left(1 + \frac{1}{K}\right) - \left(1 - \frac{1}{K}\right)\left(\frac{r}{q}\right)^3\right] \qquad (16)$$

Where p is the hydrostatic stress, β is the slope of the linear yield surface in p-t stress plane, d is the cohesion strength, r is the third invariant of the deviatoric stress, q is the von Mises equivalent stress, t is the flow stress and K is the ratio of yield stress in triaxial tension to triaxial compression. In the above equation, the K value accounts for stress path variation of shear strength under given hydrostatic pressure and determines the shape of the yield function in the deviatoric stress plane.

Apart from q and K, the flow stress 't' consists of the Lode's angle as a ratio of the third to the second invariant of the deviatoric stress [48].

For the current FE simulations, the input material properties for the Drucker-Prager plasticity model, such as β and K values are calculated using the relation between the Mohr-Coulomb and the Drucker-Prager yield criteria. According to the Mohr-Coulomb criteria, the cohesion stress c ($c \neq d$) and the angle of internal friction (ϕ) are related to the tensile (σ_{mt}) and compressive strengths (σ_{mc}) of the material by the following expression [24].

$$\sigma_{mt} = 2c\frac{\cos\phi}{1+\sin\phi}\,;\ \sigma_{mc} = 2c\frac{\cos\phi}{1-\sin\phi} \tag{17}$$

Here it should be noted that, in the absence of the neat 8552 epoxy (Hexcel) stress-strain curves, for the current numerical study, bulk epoxy stress-strain curves are used from a similar aviation grade material (8551-7 from Hexcel) [49]. *In addition, as reported in* [49] *and* [50], *both 8551-7 and 8552 bulk epoxy matrix have similar tensile and compression strength values (σ_{mt} = 99 MPa and $\sigma_{mc} = 130$ MPa).*

Corresponding to the aforesaid strength values, using Eqn 4, the internal material friction angle ϕ and the cohesion yield stress c of the epoxy were obtained as 7.78° and 56.72 MPa respectively. *As an additional validation, the computed cohesion stress value is compared to the experimental shear strength of the epoxy (57 MPa)* [50] *and a very good correlation is observed*.

With the Mohr-Coulomb internal material friction angle (ϕ), the slope of the yield surface (β) for the Drucker-Prager plasticity model is computed using the below equation [19].

$\tan\beta = \frac{6\sin\phi}{3-\sin\phi}$**Error! Digit expected.**

(18)

The above equation gives the β value of 15°. Similarly, the ratio of the triaxial tension to compression (*K)* is computed as 0.89 using the below equation [39].

$$K = \frac{3-\sin\phi}{3+\sin\phi} \quad (19)$$

Using the above discussed yield criterion, the matrix material starts to deform plastically when the yield surface is reached. Further loading produces the plastic flow in the epoxy material. Under the Drucker-Prager plasticity condition, the plastic flow (G) is defined by the following equation [48].

$$G = t - p\tan\psi \quad (20)$$

Where ψ represents the dilatation angle in the p-t stress plane. Under the conditions of the nondilatant flow rule, the ψ value is set to zero. This is due to the fact that volume changes in the yielding or post-yielding regimes have been reported to be minor for polymer materials [51].

Using the above discussed RVE modeling methodology, to avoid convergence issues caused by the interface damage and the matrix plastic deformation, the following FE simulations are accomplished in Abaqus / explicit using the direct integration method. In order to obtain a thorough understanding of various explicit solver parameters that can influence the outcome of the quasi-static computational micromechanical results, readers are referred to the recent research work of Garoz et al. [52]. In the similar guidelines of [52] [53], detailed parametric studies are conducted on various explicit parameters. Eventually, to speed up the simulation process while minimizing the errors caused by the explicit analysis, the mass scaling factor of 1E+6 is applied to the entire RVE model. The aforesaid mass scaling factor is chosen as a compromise between the speed of the numerical analysis to the accuracy of the obtained results. Moreover, to preserve the quasi-static nature of the applied loads, the kinetic energy of the whole (RVE) model is kept below 10% of the total internal energy [53], which in turn depends on the chosen mass scaling factor (1E+6) as well as the load rate ($1s^{-1}$).

3. Results and Discussion

3.1. Validating the plasticity model

For calibrating the chosen element for the FE mesh and the plasticity model for the matrix, bulk epoxy material FE simulations are accomplished under tension, compression and shear loads. For the computational purpose, a cubic geometry ($1mm^3$) is modeled using C3D8R elements. Moreover, kinematic (displacement) boundary conditions are applied to the FE model (Fig 3a) as described in Ullah et al. [18]. In order to capture the non-linear stress-strain behavior of the epoxy, along with the above computed K and β values (Table 2), the following input data is provided to the Drucker-Prager plasticity model:

i) within the linear elastic limit, Young's modulus and Poisson's ratio listed in table 1 are used; ii) beyond the elastic limit, true stress vs. true plastic strain values are derived from the experimental stress-strain curves [49] and given as an input to the plasticity model for tension and compression simulations; iii) for shear calculations, material cohesion strength (d) vs. plastic shear strain values are given as input [39]. As shown in Fig 3b, under various load conditions, the predicted stress-strain behavior matches very well with the experimental [49] bulk epoxy stress-strain curves.

3.2. RVE under transverse tension

In order to understand the effect of various material properties influencing the transverse tensile stress-strain and damage behavior of an RVE, the following important aspects related to the micromechanical FE simulations are addressed: i) initially, a parametric study is conducted to calibrate the strength and fracture energy values used for the fiber-matrix interface; ii) using the calibrated interface properties, a detailed damage analysis is conducted for the RVE under transverse tension. Here it should be highlighted that the above mentioned numerical studies are accomplished using bulk epoxy tensile stress-strain curve (Fig 3b); iii) finally, in order to estimate the effect of in-situ epoxy material properties on the predicted transverse tensile strength, RVE FE simulations are accomplished using in-situ epoxy material properties obtained from the nanoindentation testing on a carbon-epoxy composite ply [21].

3.2.1. Calibrating the mode I interface properties

Attributed to the difficulties in obtaining the interface normal strength and fracture energy values (mode I) using simple experimental testing, reliable mode I interface data is not available in the open literature. Hence, in the current research work, the mode I interface properties are evaluated through reverse engineering based on correlating the obtained RVE average stress-strain behavior to the experimental macroscopic stress-strain behavior [54]. In order to validate the RVE FE simulations, experimental macroscopic stress-strain curves are taken from [50] and [55]. *The aforementioned experimental studies are conducted on IM7/8552 UD carbon–epoxy composite material system that has a fiber volume fraction of 60%, which is similar to the RVE fiber volume fraction used for the current FE simulations.*

As explained in the above section, the cohesive elements that are used for representing the interface mechanical behavior follow the bi-linear traction separation law. Hence, in order to ensure the continuity of the stress-strain fields in the linear elastic region, an initial stiffness of 10^6 MPa/mm is assigned to the cohesive elements. For the parametric study of the interface properties, it is assumed that the transverse tensile strength of a composite ply is mainly influenced by mode I strength and fracture energy values compared to mode II interface properties [54]. Using the bulk epoxy tensile stress-strain behavior, RVE FE simulations are accomplished by varying the mode I interface strength value from 45-65 MPa (Fig 4a).

The initial guess value for the mode I fracture energy is taken as 0.04 N/mm. In addition, mode II interface strength and fracture energy values for the initial calculations are taken as 96 MPa [56] and 0.107 N/mm [57] respectively.

As shown in Fig 4a, for the chosen mode I fracture energy (0.04 N/mm) the interface strength value of approximately 60 MPa predicts the transverse tensile strength of the RVE that is in close agreement with the experimental strength. During the parametric study, it is observed that the transverse tensile strength and failure strain of a UD composite ply is a combined effect of both mode I interface strength and fracture energy values. Hence, in order to calibrate the mode I fracture energy, the interface strength value is varied around 60±5 MPa and the mode I fracture energy value is varied from 0.001 N/mm to 0.02 N/mm. From the aforementioned parametric study, the mode I interface strength of 57 *MPa* and fracture energy of *0.002 N/mm* predict the average transverse tensile strength and failure strain of the RVE that is in good agreement with the experimental stress-strain curve. As shown in Fig 4b, keeping the calibrated mode I interface strength of 57 MPa constant, the effect of interface fracture energy on the transverse tensile stress-strain behavior is shown. *From Fig 4 (a, b) one can observe that the transverse tensile strength and failure strain of an RVE is sensitive to the chosen mode I interface strength and fracture energy values.*

3.2.2. RVE under transverse tension: *micro-scale damage analysis*

The current section is devoted to present a detailed micro-scale damage analysis of the RVE under the applied transverse tensile load. Firstly, as shown in Fig 5a, a very good correlation is observed between the average stress-strain curves predicted using Abaqus built-in CZM to the cohesive zone damage model implemented using VUMAT. During the transverse tensile load application process, initially, at around 54 MPa average stress the interface damage initiation is observed (Fig 5b). As expected, the observed interface damage is mainly mode I dominant (Fig 5b). The initiation and propagation of the interface damage accelerate the plastic deformation of the epoxy strips that are bridging the neighboring interface decohesions (Fig 5c). As soon as the local equivalent stress in the epoxy strips that are connecting the neighboring interface damage reaches approximately 100 MPa (Fig 5c), RVE strain softening behavior is triggered. The aforementioned stress value corresponds to the tensile yield limit of the epoxy matrix (Fig 3b). The initiation of the strain softening process increases the epoxy strips plastic deformation and leads to the final failure of the interface elements (Fig 5d).

For validating the current numerical methodology, the obtained FE interface damage profile (Fig 6a) is compared to the experimental micro-scale damage profile (Fig 6b) [58]. The experimental micro-scale damage profile is obtained from the in-situ three-point bend test conducted on a carbon-epoxy (HTA / L135i) laminate ($[90_2/0_7/90_2]$) inside a Scanning Electron Microscope (SEM) [58]. Duri ng the experimental testing, the interface damage profile is taken on the tension side 90° ply of the laminate.

Hence, the obtained experimental damage profile closely resembles the stress state of the current transverse tension FE simulations. Fig 6 (a, b) compares the obtained FE circumferential decohesion angles (54-70°) to the experimental values (64-70°) and a good correlation is observed. In addition, as reported by Paris et al. [59][60], the above discussed interface debonding angles match very well with the interface crack kinking angle (60°-70°) into the matrix under the applied transverse tensile load.

3.2.3. RVE under transverse tension: *bulk vs. in-situ epoxy material properties*

The above discussed micromechanical FE simulations are accomplished using the *bulk epoxy non-linear stress-strain behavior* obtained from the macro-scale experiments. Hence, implicitly it is assumed that the constituent matrix material of the RVE behaves similarly compared to the bulk epoxy material. "*While it is unlikely that the fiber properties would change, there is a distinct possibility that the polymer properties could chemically change as a result of consolidation and/or cure process"*. Moreover, apart from the process induced effects, regarding the size effects, the micro-scale epoxy fiber tests conducted on RTM 6 resin (Hexcel) by Hobbiebrunken et al. [28] lead to the following observations. Due to the relevance of the experimental findings reported by [28] to the current numerical studies, in the current section the authors tried to explain the micro-scale failure behavior of the epoxy resin in a rather detailed manner: i) under the applied tensile load, almost all the resin micro fibers showed a pronounced plastic deformation with the formation of a shear band and necking before the final failure (Fig 7).

The above discussed failure process of the epoxy matrix is completely different from the brittle fracture behavior that is commonly observed from the macro-scale tension tests [26]. The above mentioned difference in the failure behavior between bulk epoxy and micro resin fibers is attributed to the average flaw size in the material under testing; ii) consequently, the size-related micro-scale matrix tensile strength is much higher (up to 55%) compared to the strength obtained from standard macro-scale test methods using bulk epoxy resin; iii) attributed to the higher in-situ strength capability of the epoxy matrix, the fiber-matrix interface debonding becomes the governing process for initial failure in composite materials and the interfacial strength becomes even more important; iv) finally, considering the size of resin pockets present in a typical fiber-reinforced composite, Hobbiebrunken et al. [28] projected that the *micro-scale epoxy strength in compression and shear will be at least 1.55 times higher than the bulk epoxy strength*.

Table 2 compares the in-situ epoxy matrix material properties measured from nanoindentation tests [21] to the bulk epoxy material properties [50]. Using the in-situ epoxy material properties, the Drucker-Prager plasticity parameters are computed and are listed in Table 2. Considering the in-situ epoxy material properties (Table 2), RVE FE simulations are accomplished under transverse tensile load and the obtained results are compared to the average stress-strain curve predicted using the bulk epoxy material properties. ***Due to the non-availability of the non-linear stress-strain curve for the in-situ epoxy matrix, elastic-perfectly plastic material behavior is assumed.***

As shown in Fig 8, the predicted transverse tensile strength of the RVE using in-situ epoxy material properties is in reasonable agreement with the strength value predicted by the RVE using bulk epoxy non-linear stress-strain curve. *Attributed to the elastic-perfectly plastic material properties used to represent the in-situ epoxy material behavior, the predicted stress-strain curve has a higher slope and hence slightly lower failure strain compared to the experimental results.*

From the above discussed comparative study, one can observe that even though the in-situ epoxy matrix tensile strength is 22 MPa higher than the bulk epoxy tensile strength, its influence on the transverse tensile strength of the RVE is negligible. The aforementioned phenomenon can be attributed to the fact that, once the interface damage initiates, the epoxy strips that are bridging the neighboring interface damage act as a load transfer material between the two halves of the RVE (Fig 6a). Attributed to the size of these epoxy strips, even a minuscule increment in the applied external load causes the stress concentration to increase sharply and reaches the tensile yield limit of the epoxy, and consequently triggering the RVE strain softening behavior. *Hence, from the above discussed interface as well as the matrix strength studies, it can be concluded that the transverse tensile strength of a UD composite ply is mainly controlled by the brittle failure behavior of the fiber-matrix interface [61]*. For more information related to the effect of matrix material failure behavior on the predicted transverse tensile stress-strain response of an RVE, readers are referred to the recently published work of the authors [61].

3.3. RVE under transverse compression

In order to understand various microscale parameters that are influencing the average compressive stress-strain behavior of an RVE, detailed numerical studies are conducted to address the following aspects: i) due to the *availability* of experimental mode II interface values for carbon-epoxy composite [56] [57], initial FE simulations are accomplished to study the effect of matrix material properties on the predicted transverse compressive stress-strain response of the RVE; ii) later, the effect of friction between the fiber/matrix interface on the predicted RVE strength is estimated; iii) finally, a detailed parametric study is conducted to estimate the effect of mode II interface strength and fracture energy values on the predicted transverse compressive stress-strain behavior.

3.3.1. RVE under transverse compression: *bulk vs. in-situ epoxy material properties*

In the process of estimating the transverse compression stress-strain behavior of a UD composite ply using micromechanical simulations, initially, RVE FE analysis is accomplished using *bulk epoxy* non-linear compression stress-strain curve (Fig 3b). Regarding interface material properties, already calibrated mode I strength (57 *MPa*) and fracture energy (*0.002 N/mm*) values are kept constant. The mode II interface strength value is taken from the experimental micro-bond tests conducted on an IM (Intermediate Modulus) carbon–epoxy (Hexcel) material system [56]. The aforesaid experiments reported the mode II interface strength value as 96±18 MPa. Hence, the mode II interface strength for the current numerical simulations is taken as 96 MPa.

The mode II interface fracture energy value is taken as 0.107 N/mm, which is experimentally measured on an IM carbon fiber-epoxy material system by Yalle et al. [57].

As shown in Fig 9a, the implemented cohesive zone damage methodology using VUMAT predicts similar stress-strain behavior compared to Abaqus built-in CZM. Moreover, one can observe that the predicted compressive strength of the RVE is approximately 40% lower compared to the experimental value (Fig 9a). A detailed study of the local stress-strain and damage profiles leads to the following observations: i) at around 130 MPa average compressive stress, the interface damage initiates; ii) as observed in the microscale transverse compression experiment of a UD CFRP composite ply [42] (Fig 9b), the current numerical methodology predicts the plastic strain localization in the epoxy matrix around the fiber-matrix interface damage (Fig 9c); iii) followed by the interface damage, at around 150 MPa average compressive stress the accumulated plastic strain in conjunction with the interface damage started to form a dominant shear band; iv) finally, in accordance with the epoxy matrix internal material friction angle ($\frac{\emptyset}{2} \cong 4^0$) combined with the RVE local fibers placement, the plastic shear band forms across the RVE at an angle of 49^0 perpendicular to the load application direction (Fig 10a). Moreover, the predicted plastic shear band angle is within the limits of the experimental shear band formation angle ($\theta_c = 53 \pm 3^0$) observed from the transverse compression tests conducted on a UD carbon-epoxy composite ply (Fig 10b) [24]. *Hence, we can conclude that the predicted micro and macroscale damage profiles are similar to the experimentally observed damage patterns.*

As shown in Fig 9a, the discrepancy between the predicted and the experimental compressive stress-strain curves can be attributed to the following two aspects of the constituent materials of the RVE: i) in-situ epoxy stress-strain behavior; ii) friction between the fiber/matrix interface. Hence, in order to investigate the effect of epoxy material properties, RVE FE simulations are accomplished using in-situ epoxy *elastic-perfectly plastic material data* (Table 2) [21]. As shown in Fig 11a, the predicted compression strength of the RVE using in-situ epoxy compression strength (176 MPa) without friction is approximately 215 MPa. Considering the experimentally reported variation in the in-situ epoxy strength (176±17 MPa), the friction coefficient between the fiber-matrix interface is varied from 0-0.4. As shown in Fig 11b, the in-situ epoxy strength of 183 MPa combined with the interface friction of 0.4 predicts the RVE compressive strength that is in good agreement with the experimental strength.

From the above discussed transverse compression simulations, it can be concluded that the in-situ compression strength of the epoxy matrix directly controls the shear band formation stress levels, and consequently influences the predicted average transverse compression strength of the RVE [42]. *Moreover, as shown in Fig 11b, attributed to the assumed elastic-perfectly plastic material behavior for the in-situ epoxy matrix, the overall stress-strain behavior of the RVE is not in good agreement with the experimental stress-strain curve. Hence, the in-situ non-linear compression stress-strain curve for the epoxy matrix is estimated by matching the RVE average stress-strain response to the experimental compressive stress-strain response of the UD composite ply.*

Using the mode II interface strength of 96 MPa and fracture energy of 0.107 N/mm, along with the estimated in-situ epoxy compression stress-strain curve (Fig 11c), the predicted average compressive stress-strain behavior of the RVE (Fig 11d) is in reasonable agreement with the experimental results. Finally, combining the estimated in-situ epoxy curve (Fig 11c) with a friction coefficient of 0.4, the predicted RVE compressive strength and failure strain are in good agreement with the experimental results. As shown in Fig 11d, incorporating the friction coefficient increases the compression strength of the RVE by approximately 13 MPa. Finally, as shown in Fig 11c, one can observe that the predicted in-situ compression strength value of the epoxy matrix is approximately 60% higher than the bulk epoxy compression strength, which is in line with the projected compression strength value for in-situ epoxy reported by Hobbiebrunken et al. [28].

As discussed above, the RVE ductile stress-strain behavior under the applied transverse compression load is not only influenced by the in-situ matrix properties but also depends on mode II interface strength and fracture energy values. Hence, using the predicted in-situ epoxy stress-strain curve (Fig 11c), a detailed parametric study is conducted. For the current numerical studies, mode II interface strength value is varied from 40 MPa to 120 MPa, while keeping the mode II fracture energy constant at 0.107 N/mm. As shown in Fig 12a, the interface strength value has a significant influence on the predicted failure stress, strain and the overall ductile stress-strain behavior of the RVE.

Moreover, from Fig 12a one can observe that the interface strength values above 100 MPa predict almost similar stress-strain response. Besides the mode II interface strength, interface fracture energy can influence the average stress-strain behavior. In order to investigate the influence of interface fracture energy on the average compressive stress-strain behavior, the experimentally measured interface strength of 96 MPa is kept constant, and the interface fracture energy value is varied from 0.05 N/mm to 0.2 N/mm. As shown in Fig 12b, except at lower interface fracture energies (< 0.05 N/mm), all the predicted stress-strain curves with other fracture energies almost converged to the experimental stress-strain curve.

3.4. RVE under in-plane shear load

In order to predict the in-plane shear stress-strain response of a UD composite ply using micromechanical FE simulations, numerically calibrated mode I and experimental mode II interface strength and fracture energy values (Table 3) are used. As shown in Fig 13a, the predicted in-plane shear strength of the RVE using bulk epoxy shear stress-strain curve is approximately 43% lower than the experimental shear strength. Moreover, one can observe that the predicted RVE average shear strength (57 MPa) (Fig 13a) is similar to the computed bulk epoxy cohesion strength. Hence, as explained above (RVE under transverse compression), in order to predict the *in-situ shear stress-strain behavior* of the epoxy, RVE in-plane shear simulations are accomplished by matching the predicted average stress-strain response to the experimental in-plane shear stress-strain behavior.

Fig 13b shows the in-situ shear stress-strain behavior of the epoxy in comparison to the bulk epoxy shear stress-strain behavior. Finally, Fig 13c shows the comparison between the experimental [50] vs. numerical in-plane shear stress-strain response of the RVE.

4. Predicting the bi-axial failure envelope

To achieve the goal of the current research work, using the interface mechanical properties listed in Table 3 along with the estimated in-situ epoxy stress-strain curves, the RVE is subjected to bi-axial loading in σ_{22}-τ_{12} plane. Each point in the predicted failure envelope (Fig 14) corresponds to a particular ratio of transverse (tension/compression) to in-plane shear displacement. In addition, the predicted failure envelope is marked based on the observed dominant failure mode under the applied bi-axial load. As shown in Fig 14, the effect of the interface friction coefficient is negligible in the tension dominated region of the failure envelope. However, in the shear dominated failure region, the interface friction coefficient shows a minor influence. In contrast, one can observe that the increase in friction coefficient from 0.2-0.4 causes the increase in the bi-axial strength of the RVE in the compression dominated region. Nevertheless, increasing the friction coefficient from 0.4-0.6 does not show a significant influence on the bi-axial strength of the RVE. Finally, Fig 15 (a, b) shows the failure profiles of the RVE in the combined transverse tension-in-plane shear and transverse compression-in-plane shear dominated stress space respectively.

5. Conclusions

A comprehensive micromechanics based FE analysis methodology is presented to predict the bi-axial failure envelope of a UD composite ply in the matrix dominated directions. A coupled numerical-experimental methodology is employed to predict and calibrate the interface and in-situ epoxy properties. In order to include the frictional sliding between fiber-matrix interface, cohesive zone damage methodology combined with the Coulomb frication law is implemented into Abaqus /explicit using VUMAT. Under individual load cases, the obtained damage profiles and stress-strain curves are compared to the experimental results. Finally, the thoroughly validated numerical methodology under uniaxial load cases is extended to predict the bi-axial failure envelope of a UD composite ply. Detailed micromechanical studies related to various material parameters that are influencing the strength and failure strain predictions of the RVE lead to the following conclusions:

i) From the above presented numerical methodology, one can observe that the chosen matrix material properties have a minor influence on the predicted transverse tensile strength of the RVE. Hence, using the bulk epoxy non-linear stress-strain behavior as an anchor point, mode I interface strength and fracture energy values are calibrated.

ii) Under the applied transverse tensile load, the predicted homogenized strength and failure strain, as well as the brittle failure behavior of the RVE are mainly influenced by mode I interface strength and fracture energy values.

iii) In contrast, transverse compression and in-plane shear stress-strain behavior of the RVE is mainly influenced by the in-situ epoxy stress-strain behavior. Hence, keeping the experimental mode II interface strength and fracture energy values as anchor points, the in-situ compression and in-plane shear stress-strain response of the epoxy matrix is estimated.

iv) Similar to the conclusion of [28] [29] [62], the predicted in-situ compression and shear strength of the epoxy matrix is much higher than the bulk epoxy strength, which is directly controlling the compression and in-plane shear stress-strain behavior of the RVE.

v) By observing the failure behavior of the RVE under biaxial loads, it can be concluded that under the combined transverse tension - in-plane shear loads, the failure behavior of the RVE is mainly controlled by the mode I interface strength values.

vi) Under transverse compression - in-plane shear loads, the yield behavior of the RVE is mainly controlled by the in-situ strength of the epoxy matrix.

vii) The friction between the fiber-matrix interface shows a considerable influence on the predicted strength values under biaxial loads, especially, under transverse compression-in-plane shear dominated stress space.

viii) After conducting a detailed study regarding the influence of various microscale parameters on the macroscopic stress-strain behavior, the future research work in this area should focus on the following aspects: a) understanding the in-situ epoxy yield behavior under shear as well as combined loads; b) experimental evaluation of mode I interface properties.

Table 1. *CFRP UD ply constituent level elastic properties*[42][50]

Property	Carbon fiber	8552 epoxy Resin
Longitudinal modulus E11 [GPa]	238	4.08
Transverse modulus E22, E33 [GPa]	28	
Poisson's ratio nu12, nu13 [-]	0.28	0.38
Shear modulus G12, G13 [GPa]	24	-
Shear modulus G23 [GPa]	7.2	-

Table 2. *Comparison between epoxy material properties obtained from different experimental techniques at different length scales.*

	Bulk epoxy [50]	Epoxy (micro-scale) fiber test [28]	In-situ epoxy test (nanoindentation) [21]
Elastic Modulus [GPa]	4.08	-	5.07
Poisson's ratio [-]	0.38	-	0.35
Tensile strength [MPa]	99	135±21	121
Compression strength [MPa]	130	-	176±17
Cohesion stress (c)* [MPa]	***57***	**-**	***73***
Ratio of tri-axial tension to tri-axial compression*, K [-]	***0.91***	**-**	***0.89***
Slope of the yield surface*, β [-]	***15.73***	**-**	***21.53***

*Computed values using the relation between the Mohr-coulomb and the Drucker-Prager plasticity criterion.

Table 3. *Calibrated and experimental* [56] [57] *fiber-matrix interface properties for the IM7/8552 carbon–epoxy material system.*

Property	Mode I	Mode II /Mode III
Interface strength [MPa]	57	96
Interface fracture energy [N/mm]	0.002	0.107

6. References

[1] Z. Hashin, “Failure Criteria for Unidirectional fiber composites,” *J. Appl. Mech.*, vol. 47, no. June, pp. 329–334, 1980.

[2] C. R.M., “Stress based yield/failure criteria for fiber composites,” vol. 34, no. 5, pp. 529–543, 1997.

[3] J. Tao, “Prediction of failure envelopes and stress/strain behaviour of composite laminates,” *Compos. Sci. Technol.*, vol. 58, no. 7, pp. 1125–1136, 1998.

[4] C. T. Sun, J. Tao, and A. S. Kaddour, “The prediction of failure envelopes and stress/strain behavior of composite laminates: Comparison with experimental results,” *Fail. Criteria Fibre-Reinforced-Polymer Compos.*, vol. 62, pp. 890–902, 2004.

[5] L. J. Hart-Smith, “Maximum-Strain Failure Models for Certain Fibrous Composite Laminates,” *Compos. Sci. Technol.*, vol. 58, no. 7, pp. 1151–1178, 1998.

[6] R. M. Christensen, “Tensor Transformations and Failure Criteria for the Analysis of Fiber Composite Materials,” *J. Compos. Mater.*, vol. 22, no. 9, pp. 874–897, 1988.

[7] A. Puck and H. Schürmann, “Failure analysis of FRP laminates by means of physically based phenomenological models *,” pp. 264–297, 2004.

[8] C. G. Dávila, P. P. Camanho, and C. A. Rose, “Failure criteria for FRP laminates,” *J. Compos. Mater.*, vol. 39, no. 4, pp. 323–345, 2005.

[9] S. T. Pinho, L. Iannucci, and P. Robinson, “Physically based failure models and criteria for laminated fibre-reinforced composites with emphasis on fibre kinking. Part I: FE implementation,” *Compos. Part A Appl. Sci. Manuf.*, vol. 37, no. 5, pp. 63–73, 2006.

[10] S. T. Pinho, C. G. Dávila, P. P. Camanho, L. Iannucci, and P. Robinson, “Failure Models and Criteria for FRP Under In-Plane or Three-Dimensional Stress States Including Shear Non-linearity,” *Nasa/Tm-2005-213530*, no. February, p. 68, 2005.

[11] P. D. Soden, M. J. Hinton, and A. S. Kaddour, “Lamina properties, lay-up configurations and loading conditions for a range of fibre reinforced composite laminates,” in *Failure Criteria in Fibre-Reinforced-Polymer Composites*, 2004, pp. 30–51.

[12] M. J. Hinton, A. S. Kaddour, and P. D. Soden, “A comparison of the predictive capabilities of current failure theories for composite laminates, judged against experimental evidence,” *Compos. Sci. Technol.*, vol. 64, no. 3–4, pp. 549–588, 2004.

[13] P. D. Soden, M. J. Hinton, and A. S. Kaddour, “Biaxial test results for strength and deformation of a range of E-glass and carbon fibre reinforced composite laminates : failure exercise benchmark data,” vol. 62, pp. 1489–1514, 2002.

[14] Q. Sun *et al.*, “Failure criteria of unidirectional carbon fi ber reinforced polymer composites informed by a computational micromechanics model,” *Compos. Sci. Technol.*, vol. 172, no. December 2018, pp. 81–95, 2019.

[15] I. M. Daniel, J. J. Luo, P. M. Schubel, and B. T. Werner, “Interfiber/interlaminar failure of composites under multi-axial states of stress,” *Compos. Sci. Technol.*, vol. 69, no. 6, pp. 764–771, 2009.

[16] J. D. Schaefer, B. T. Werner, and I. M. Daniel, “Strain-Rate-Dependent Failure of a Toughened Matrix Composite,” *Exp. Mech.*, vol. 54, no. 6, pp. 1111–1120, 2014.

[17] C. Varga, N. Miskolczi, L. Bartha, and G. Lipóczi, “Improving the mechanical properties of glass-fibre-reinforced polyester composites by modification of fibre surface,” *Mater. Des.*, vol. 31, no. 1, pp. 185–193, 2010.

[18] Z. Ullah, L. Kaczmarczyk, and C. J. Pearce, “Three-dimensional nonlinear micro/meso-mechanical response of the fibre-reinforced polymer composites,” *Compos. Struct.*, vol. 161, pp. 204–214, 2017.

[19] L. Yang, Y. Yan, Y. Liu, and Z. Ran, “Microscopic failure mechanisms of fiber-reinforced polymer composites under transverse tension and compression,” *Compos. Sci. Technol.*, vol. 72, no. 15, pp. 1818–1825, 2012.

[20] E. Totry, C. González, and J. LLorca, “Failure locus of fiber-reinforced composites under transverse compression and out-of-plane shear,” *Compos. Sci. Technol.*, vol. 68, no. 3–4, pp. 829–839, 2008.

[21] F. Naya, C. González, C. S. Lopes, S. Van der Veen, and F. Pons, “Computational micromechanics of the transverse and shear behavior of unidirectional fiber reinforced polymers including environmental effects,” *Compos. Part A Appl. Sci. Manuf.*, vol. 92, pp. 146–157, 2017.

[22] E. Totry, J. M. Molina-Aldareguía, C. González, and J. LLorca, “Effect of fiber, matrix and interface properties on the in-plane shear deformation of carbon-fiber reinforced composites,” *Compos. Sci. Technol.*, vol. 70, no. 6, pp. 970–980, 2010.

[23] L. P. Canal, C. González, J. Segurado, and J. LLorca, “Intraply fracture of fiber-reinforced composites: Microscopic mechanisms and modeling,” *Compos. Sci. Technol.*, vol. 72, no. 11, pp. 1223–1232, 2012.

[24] C. González and J. LLorca, “Mechanical behavior of unidirectional fiber-reinforced polymers under transverse compression: Microscopic mechanisms and modeling,” *Compos. Sci. Technol.*, vol. 67, no. 13, pp. 2795–2806, 2007.

[25] T. J. Vaughan and C. T. McCarthy, “Micromechanical modelling of the transverse damage behaviour in fibre reinforced composites,” *Compos. Sci. Technol.*, vol. 71, no. 3, pp. 388–396, 2011.

[26] B. Fiedler, M. Hojo, S. Ochiai, K. Schulte, and M. Ando, “Failure behavior of an epoxy matrix under different kinds of static loading,” *Compos. Sci. Technol.*, vol. 61, no. 11, pp. 1615–1624, 2001.

[27] A. Arteiro, G. Catalanotti, A. R. Melro, P. Linde, and P. P. Camanho, “Micro-mechanical analysis of the in situ effect in polymer composite laminates,” *Compos. Struct.*, vol. 116, no. 1, pp. 827–840, 2014.

[28] T. Hobbiebrunken, B. Fiedler, M. Hojo, and M. Tanaka, “Experimental determination of the true epoxy resin strength using micro-scaled specimens,” *Compos. Part A Appl. Sci. Manuf.*, vol. 38, no. 3, pp. 814–818, 2007.

[29] J. R. Gregory and S. M. Spearing, “Nanoindentation of neat and in situ polymers in polymer-matrix composites,” *Compos. Sci. Technol.*, vol. 65, no. 3–4, pp. 595–607, 2005.

[30] M. Hardiman, T. J. Vaughan, and C. T. McCarthy, “Fibrous composite matrix characterisation using nanoindentation: The effect of fibre constraint and the evolution from bulk to in-situ matrix properties,” *Compos. Part A Appl. Sci. Manuf.*, vol. 68, pp. 296–303, 2015.

[31] S. Wang, Y. Yang, L. M. Zhou, and Y. W. Mai, “Size effect in microcompression of epoxy micropillars,” *J. Mater. Sci.*, 2012.

[32] G. Catalanotti, C. Furtado, T. Scalici, G. Pitarresi, F. P. van der Meer, and P. P. Camanho, “The effect of through-thickness compressive stress on mode II interlaminar fracture toughness,” *Compos. Struct.*, vol. 182, no. June, pp. 153–163, 2017.

[33] H. Körber, “Mechanical response of advanced composites under high strain rates,” Universidade do Porto, 2012.

[34] M. Naderi, N. Apetre, and N. Iyyer, “Effect of interface properties on transverse tensile response of fiber-reinforced composites: Three-dimensional micromechanical modeling,” *J. Compos. Mater.*, vol. 51, no. 21, pp. 2963–2977, 2017.

[35] C. Marsden, M. Biercacki, C. Li, and S. Carnegie, “4-Point Bending Fatigue of Thin Carbon-Epoxy Laminates,” *19 Th Int. Conf. Compos. Mater.*, 2013.

[36] E. Totry, C. González, and J. LLorca, “Prediction of the failure locus of C/PEEK composites under transverse compression and longitudinal shear through computational micromechanics,” *Compos. Sci. Technol.*, vol. 68, no. 15–16, pp. 3128–3136, 2008.

[37] M. Naderi and N. Iyyer, “Micromechanical analysis of damage mechanisms under tension of 0°–90° thin-ply composite laminates,” *Compos. Struct.*, vol. 234, no. November 2019, p. 111659, 2020.

[38] S. Daggumati, A. Sharma, and Y. S. Pydi, “Micromechanical FE Analysis of SiCf/SiC Composite with BN Interface,” *Silicon*, no. https://doi.org/10.1007/s12633-019-00119-3, Feb. 2019.

[39] “ABAQUS (2010) Analysis User’s Manual. Version 6.10,” *Dassault Systemes Simulia, Inc.* .

[40] G. Alfano and E. Sacco, “Combining interface damage and friction in a cohesive-zone model,” *Int. J. Numer. Methods Eng.*, vol. 68, no. 5, pp. 542–582, 2006.

[41] F. P. Van Der Meer and L. J. Sluys, “A numerical investigation into the size effect in the transverse crack tension test for mode II delamination,” *Compos. Part A Appl. Sci. Manuf.*, vol. 54, pp. 145–152, 2013.

[42] J. Chevalier, P. P. Camanho, F. Lani, and T. Pardoen, “Multi-scale characterization and modelling of the transverse compression response of unidirectional carbon fiber reinforced epoxy,” *Compos. Struct.*, vol. 209, no. October 2018, pp. 160–176, 2019.

[43] A. Turon, E. V. González, C. Sarrado, G. Guillamet, and P. Maimí, “Accurate simulation of delamination under mixed-mode loading using a cohesive model with a mode-dependent penalty stiffness,” *Compos. Struct.*, vol. 184, no. September 2017, pp. 506–511, 2018.

[44] J. KOYANAGI, P. D. SHAH, S. KIMURA, S. K. HA, and H. KAWADA, “Mixed-Mode Interfacial Debonding Simulation in Single-Fiber Composite under a Transverse Load,” *J. Solid Mech. Mater. Eng.*, vol. 3, pp. 1880–9871, 2008.

[45] P. Camanho and C. G. Davila, “Mixed-Mode Decohesion Finite Elements in for the Simulation Composite of Delamination Materials,” 2002.

[46] M. L. Benzeggagh and M. Kenane, “Measurement of Mixed-Mode Delamination Fracture Toughness of Unidirectional Glass / Epoxy Composites With Mixed-Mode Bending Apparatus,” vol. 56, pp. 439–449, 1996.

[47] L. E. Asp, L. A. Berglund, and R. Talreja, “A criterion for crack initiation in glassy polymers subjected to a composite-like stress state,” *Compos. Sci. Technol.*, vol. 56, no. 11, pp. 1291–1301, 1996.

[48] J. F. Jiang and Y. F. Wu, “Identification of material parameters for Drucker-Prager plasticity model for FRP confined circular concrete columns,” *Int. J. Solids Struct.*, vol. 49, no. 3–4, pp. 445–456, 2012.

[49] A. S. Kaddour and M. J. Hinton, “Input data for test cases used in benchmarking triaxial failure theories of composites,” *J. Compos. Mater.*, vol. 46, no. 19–20, pp. 2295–2312, 2012.

[50] A. S. Kaddour, M. J. Hinton, P. A. Smith, and S. Li, “Mechanical properties and details of composite laminates for the test cases used in the third world-wide failure exercise,” *J. Compos. Mater.*, vol. 47, no. 20–21, pp. 2427–2442, 2013.

[51] S. Zike, L. P. Mikkelsen, B. F. Sørensen, and V. Tvergaard, *Micro - Scale Experiments and Models for Composite Materials with Materials Research*. DTU Wind Energy PhD Thesis 2015, 2015.

[52] D. Garoz *et al.*, “Consistent application of periodic boundary conditions in implicit and explicit finite element simulations of damage in composites,” *Compos. Part B*, vol. 168, no. December 2018, pp. 254–266, 2019.

[53] G. Venu Gopala Rao, P. Mahajan, and N. Bhatnagar, “Machining of UD-GFRP composites chip formation mechanism,” *Compos. Sci. Technol.*, vol. 67, no. 11–12, pp. 2271–2281, 2007.

[54] Q. Sun *et al.*, “Multi-scale computational analysis of unidirectional carbon fiber reinforced polymer composites under various loading conditions,” *Compos. Struct.*, vol. 196, no. May, pp. 30–43, 2018.

[55] H. Koerber *et al.*, “Experimental characterization and constitutive modeling of the non-linear stress–strain behavior of unidirectional carbon–epoxy under high strain rate loading,” *Adv. Model. Simul. Eng. Sci.*, vol. 5, no. 1, 2018.

[56] B. Yu, Z. Jiang, X. Z. Tang, C. Y. Yue, and J. Yang, “Enhanced interphase between epoxy matrix and carbon fiber with carbon nanotube-modified silane coating,” *Compos. Sci. Technol.*, vol. 99, pp. 131–140, 2014.

[57] R. B. Yallee and R. J. Young, “Evaluation of interface fracture energy for single-fibre composites,” *Compos. Sci. Technol.*, vol. 58, no. 12, pp. 1907–1916, 1998.

[58] T. Hobbiebrunken, M. Hojo, T. Adachi, C. De Jong, and B. Fiedler, “Evaluation of interfacial strength in CF/epoxies using FEM and in-situ experiments,” *Compos. Part A Appl. Sci. Manuf.*, vol. 37, no. 12, pp. 2248–2256, 2006.

[59] P. L. Zumaquero, E. Correa, J. Justo, and F. París, “Microscopical observations of interface cracks from inter-fibre failure under compression in composite laminates,” *Compos. Part A Appl. Sci. Manuf.*, vol. 110, no. September 2017, pp. 76–83, 2018.

[60] F. París, E. Correa, and V. Mantič, “Kinking of Transversal Interface Cracks Between Fiber and Matrix,” *J. Appl. Mech.*, vol. 74, no. July 2007, p. 703, 2007.

[61] A. Sharma and S. Daggumati, “Computational micromechanical modeling of transverse tensile damage behavior in unidirectional glass fiber-reinforced plastic composite plies : Ductile versus brittle fracture mechanics approach,” *Int. J. Damage Mech.*, vol. 0, no. 0, pp. 1–22, 2019.

[62] M. Romanowicz, “Determination of the first ply failure load for a cross ply laminate subjected to uniaxial tension through computational micromechanics,” *Int. J. Solids Struct.*, vol. 51, no. 13, pp. 2549–2556, 2014.

a)

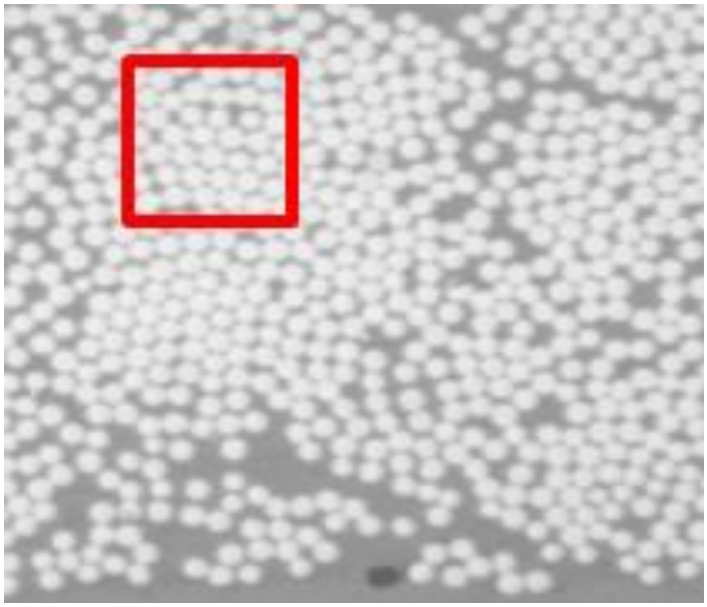

b)

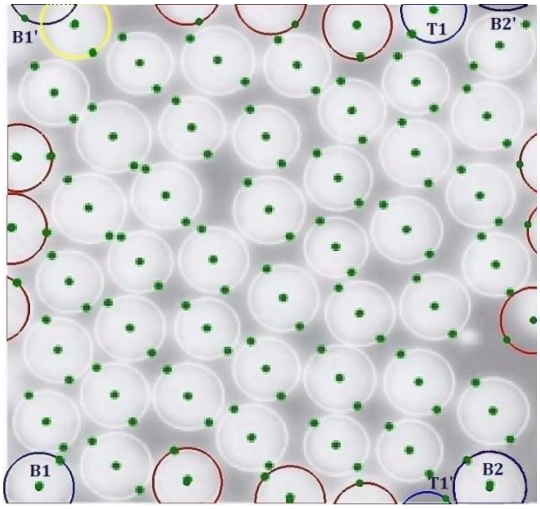

c)

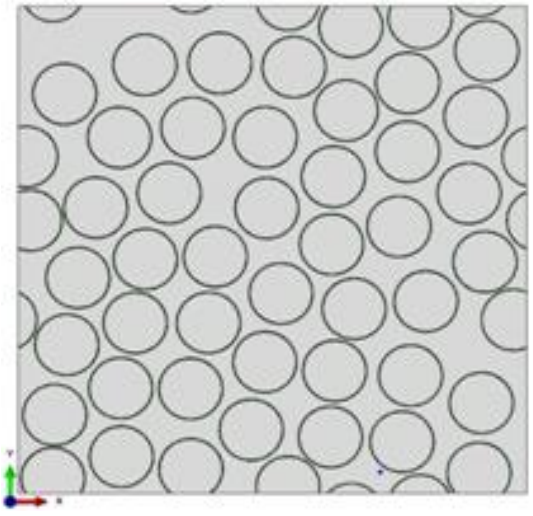

d)

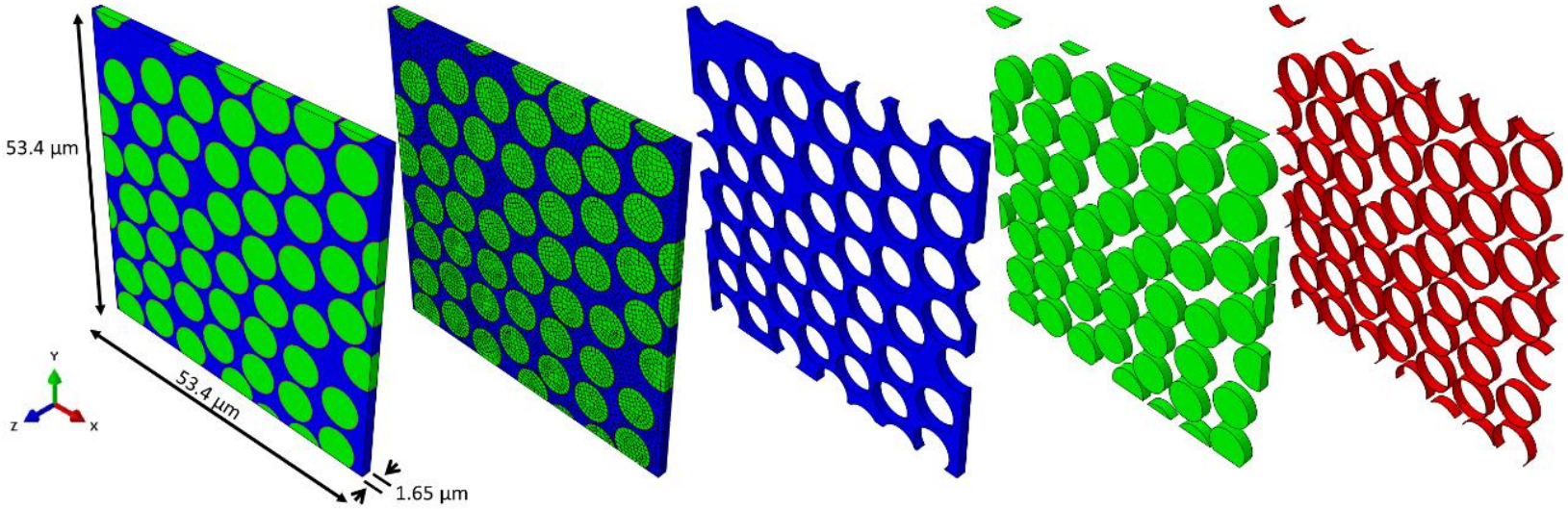

Fig 1. RVE model generation based on the microstructure: a) fiber distribution in a 90^0 ply of a UD composite [35]; b) fibers highlighted showing the centroid and the diameter (edge fibers are highlighted to show the periodicity); c) RVE geometrical model; d) RVE with different constituent materials.

a)

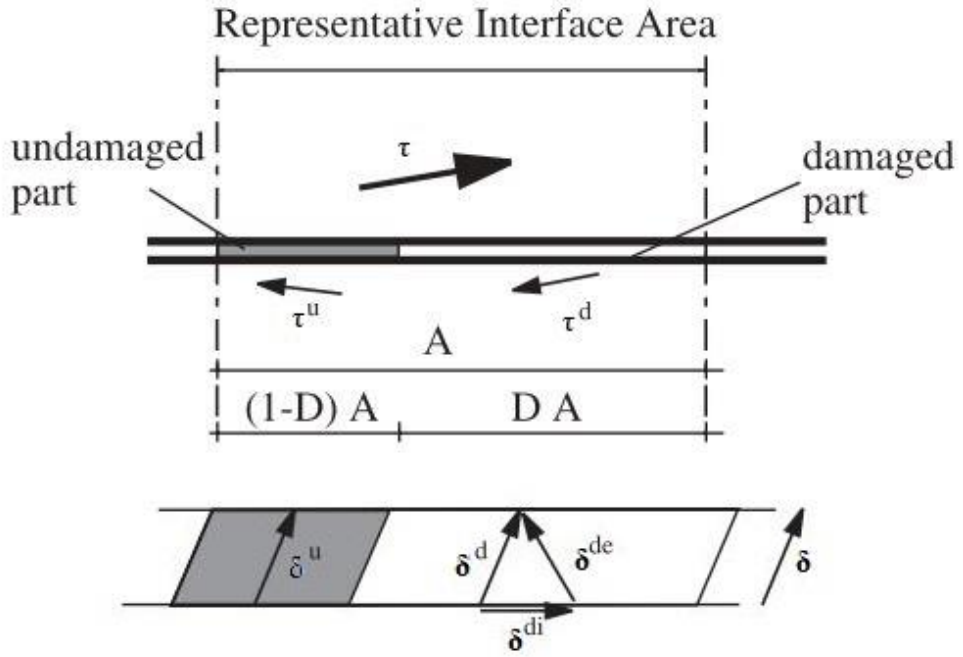
Representative Interface Area
undamaged part
damaged part
τ
τ^u
τ^d
A
(1-D) A
D A
δ^u
δ^d
δ^de
δ
δ^di

b)

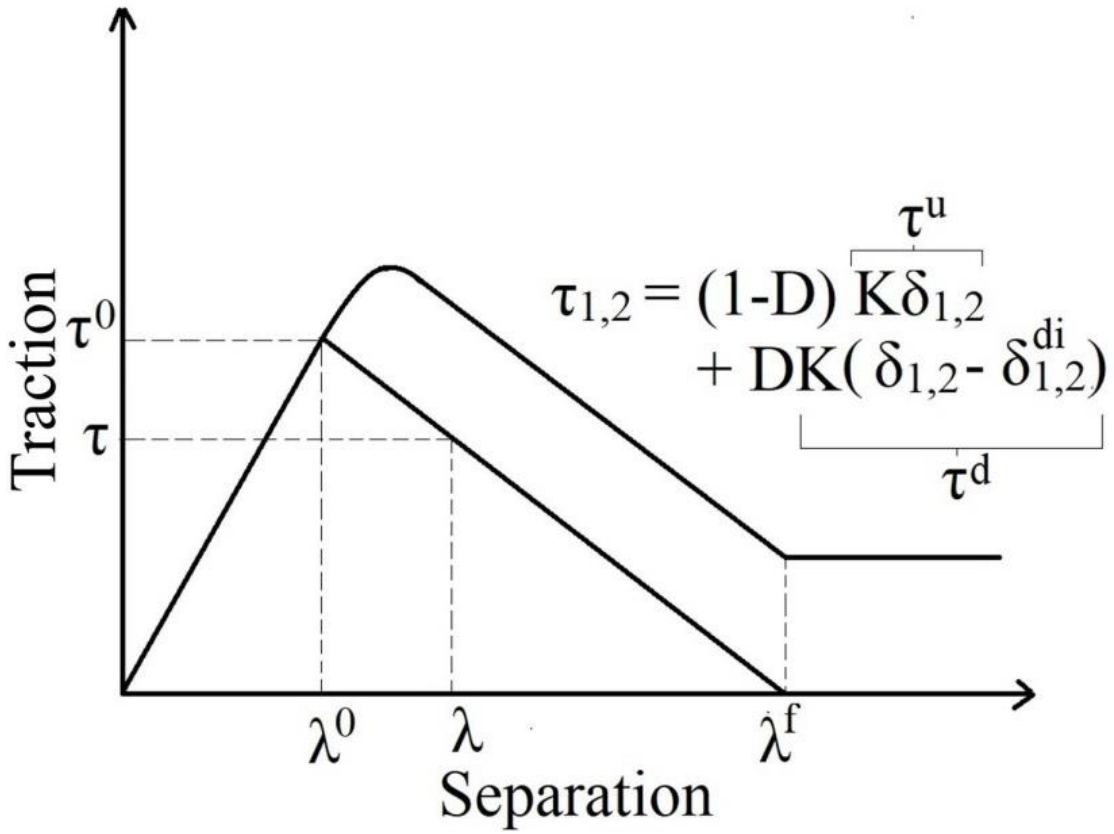
Traction
τ^0
τ
λ^0
λ
λ^f
Separation
τ^u
τ_1,2 = (1-D) Kδ_1,2
+ DK(δ_1,2 - δ^di_1,2)
τ^d

c)

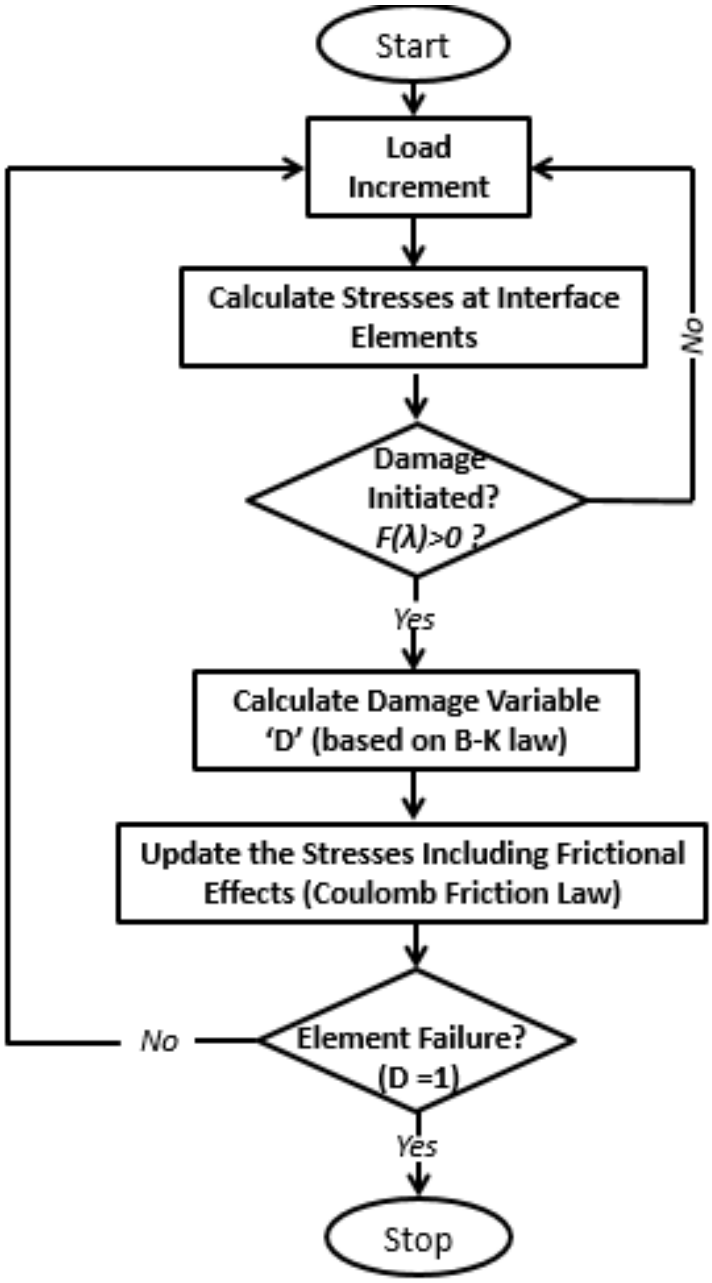

Fig 2. Interface damage model coupled with friction: a) Representative Elementary Area [40]; b) graphical representation of the traction-separation law combined with friction [41]; c) flow-chart of the implemented interface damage model combined with Columb friction law.

a)

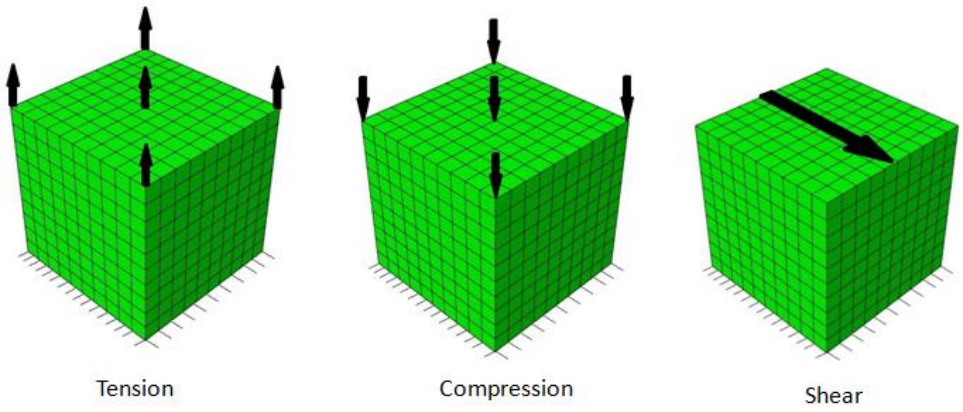

b)

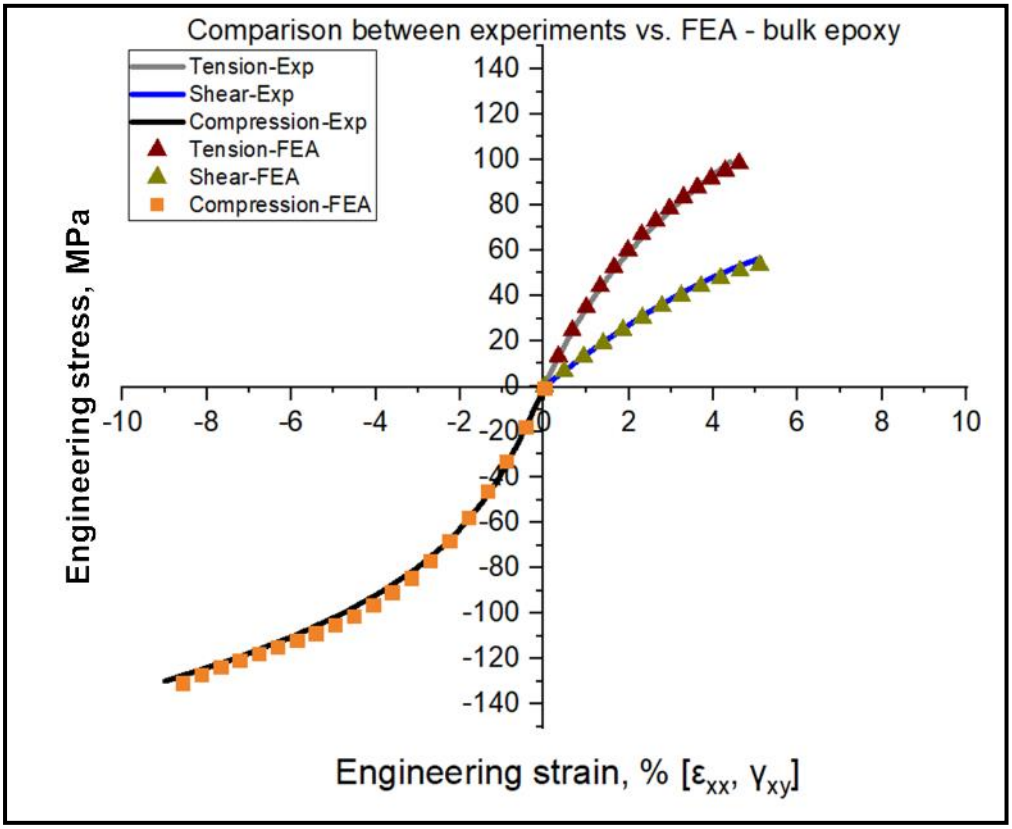

Fig 3. Calibrating the matrix material model: a) geometry and boundary conditions for bulk epoxy FE simulations; b) comparison between the experimental [49] and FE stress-strain curves.

a)

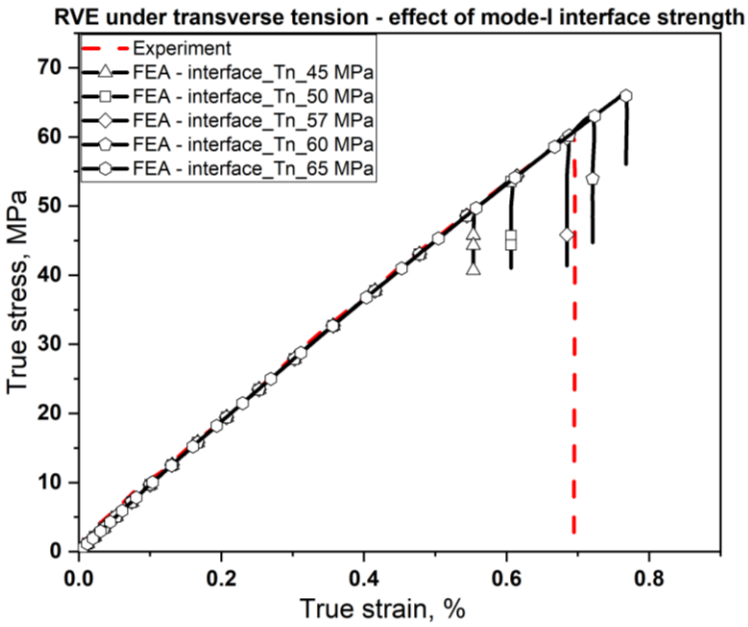

b)

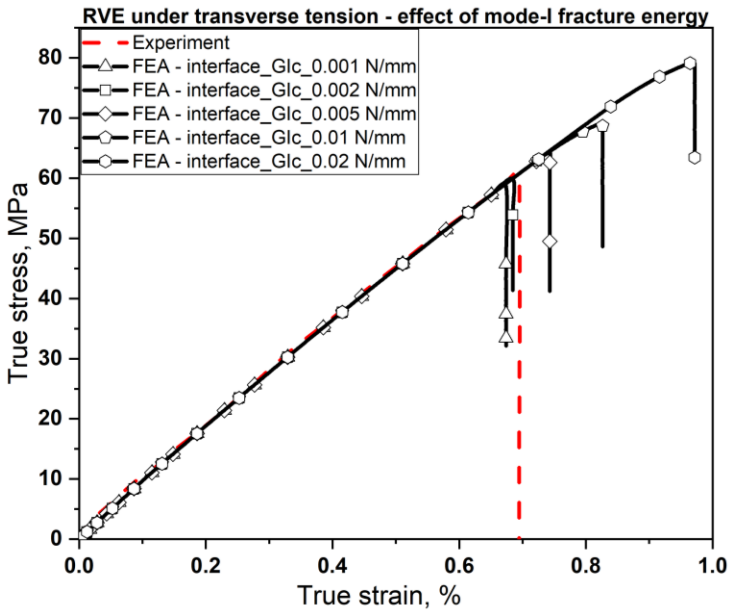

Fig 4. Calibrating mode I interface strength and fracture energy values: a) effect of mode I interface strength on the transverse tension stress-strain behavior; b) effect of mode I interface fracture energy on the transverse tension stress-strain behavior;

a)

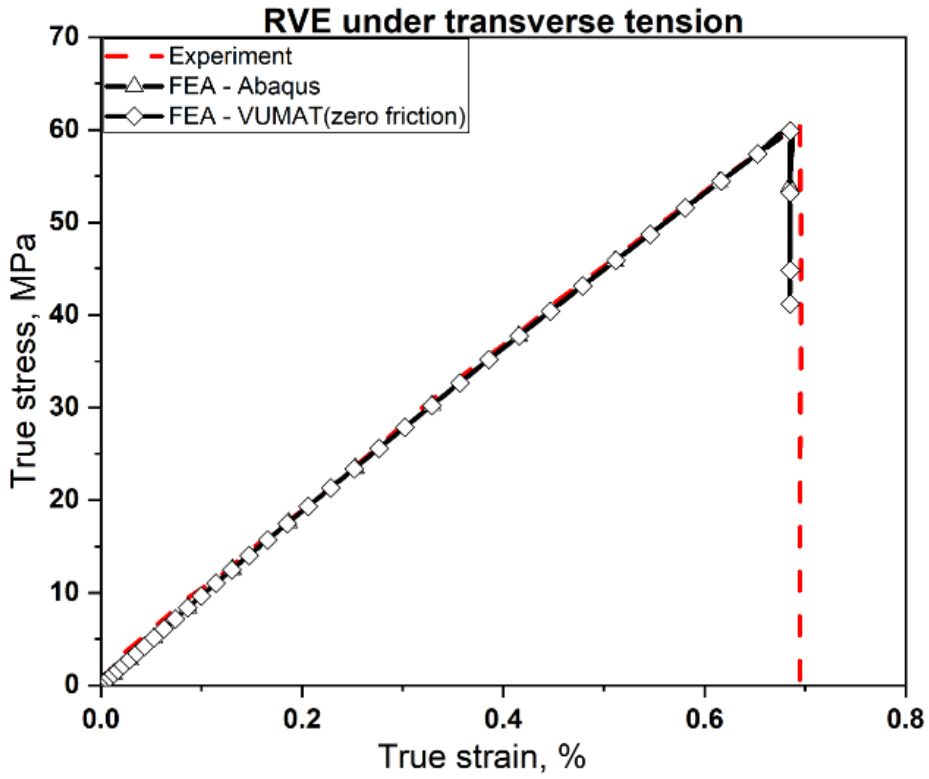
RVE under transverse tension
Experiment
FEA - Abaqus
FEA - VUMAT(zero friction)
True stress, MPa
True strain, %
0
10
20
30
40
50
60
70
0.0
0.2
0.4
0.6
0.8

b)

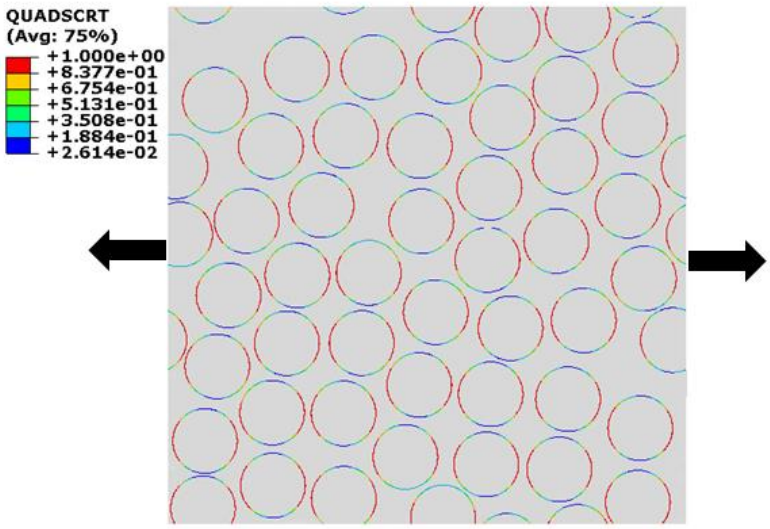
QUADSCRT
(Avg: 75%)
+1.000e+00
+8.377e-01
+6.754e-01
+5.131e-01
+3.508e-01
+1.884e-01
+2.614e-02

c)

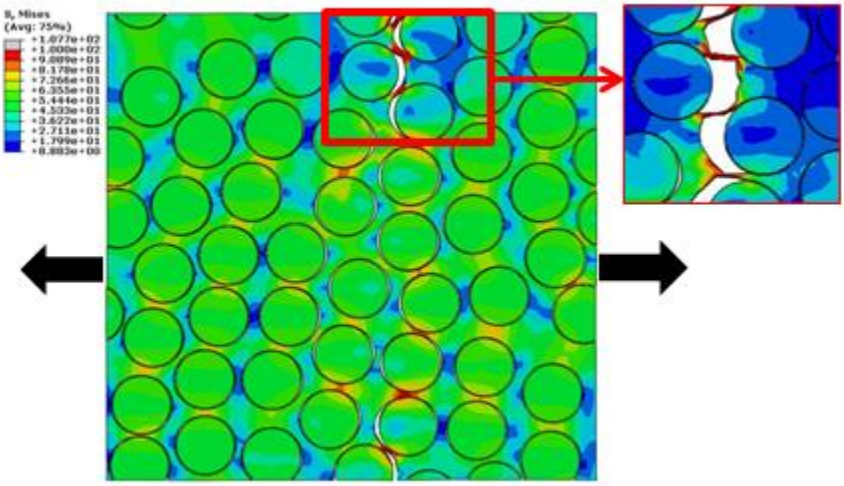

d)

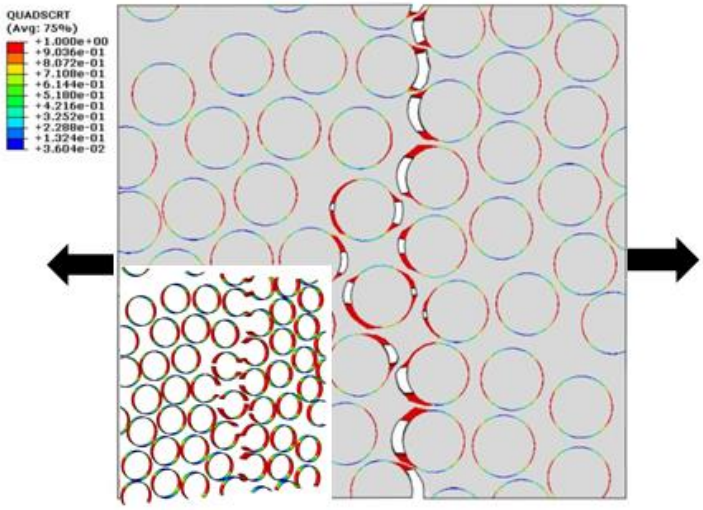

Fig 5. RVE under transverse tension: a) comparison between the experimental [55] and numerical stress-strain curve; b) mode I interface damage in the RVE; c) RVE interface damage profile in combination with the epoxy strips plastic deformation; d) failure of the interface cohesive elements.

a)

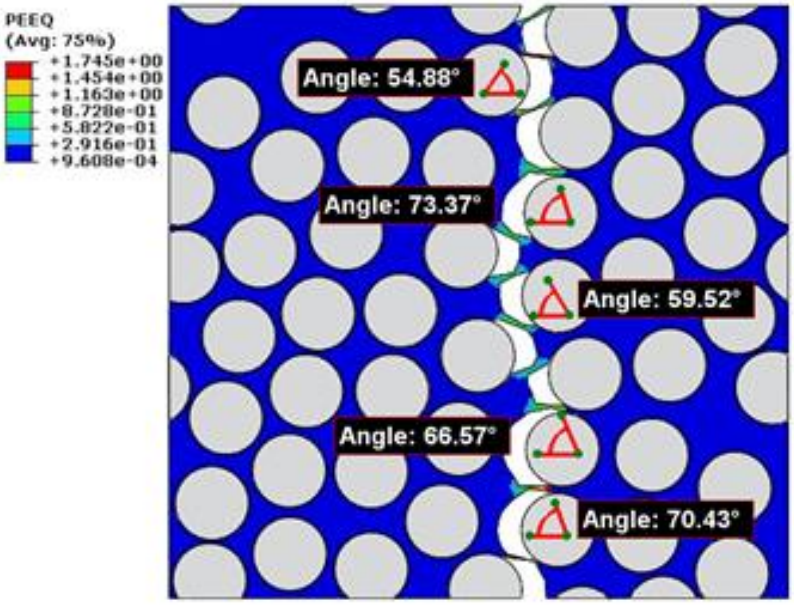

b)

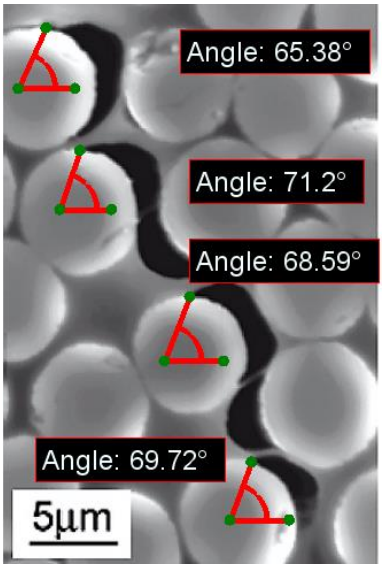

Fig 6. Comparison between numerical and experimental [58] interface damage profile: a) measured FEA circumferential interface crack opening angle; b) experimental circumferential interface crack opening angle [58].

a)

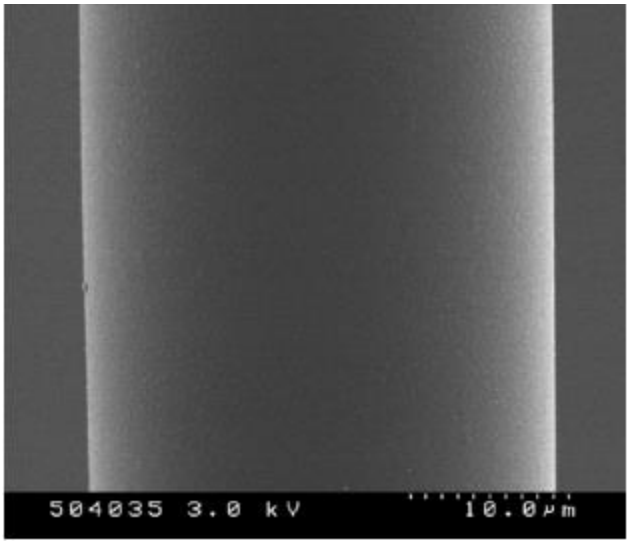

b)

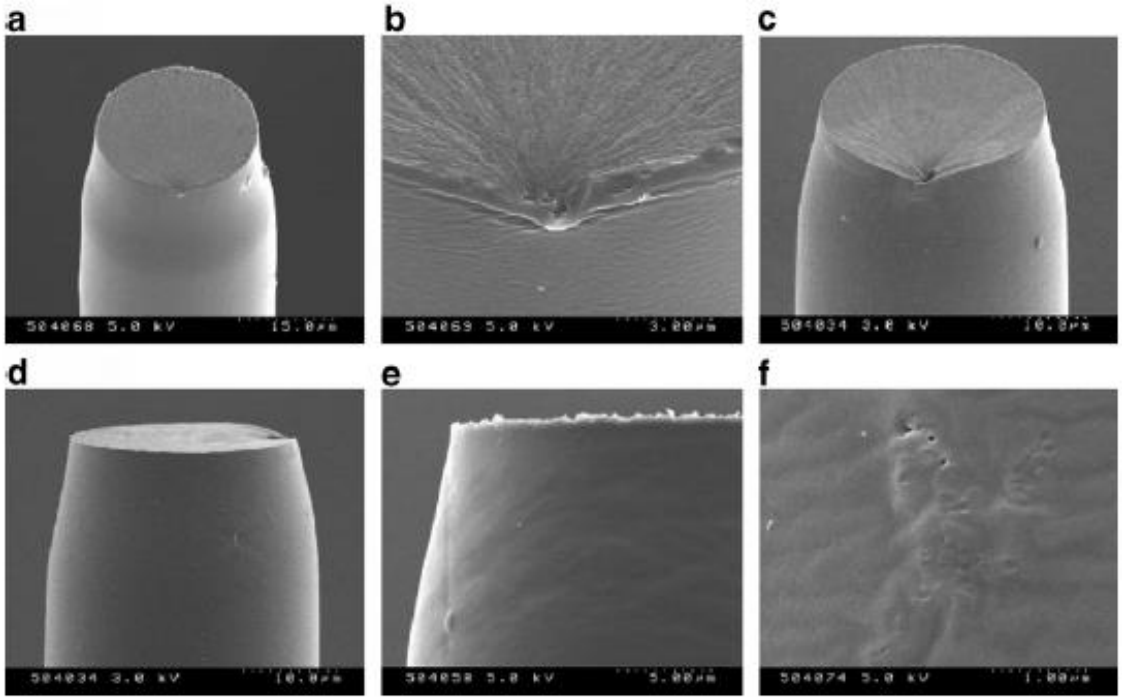

Fig 7. Ductile failure behavior of the epoxy fibers under tensile load [28]: a) resin fiber before loading (average diameter ~36.7µm); b) microscopic images showing necking and failure surfaces of the epoxy fibers.

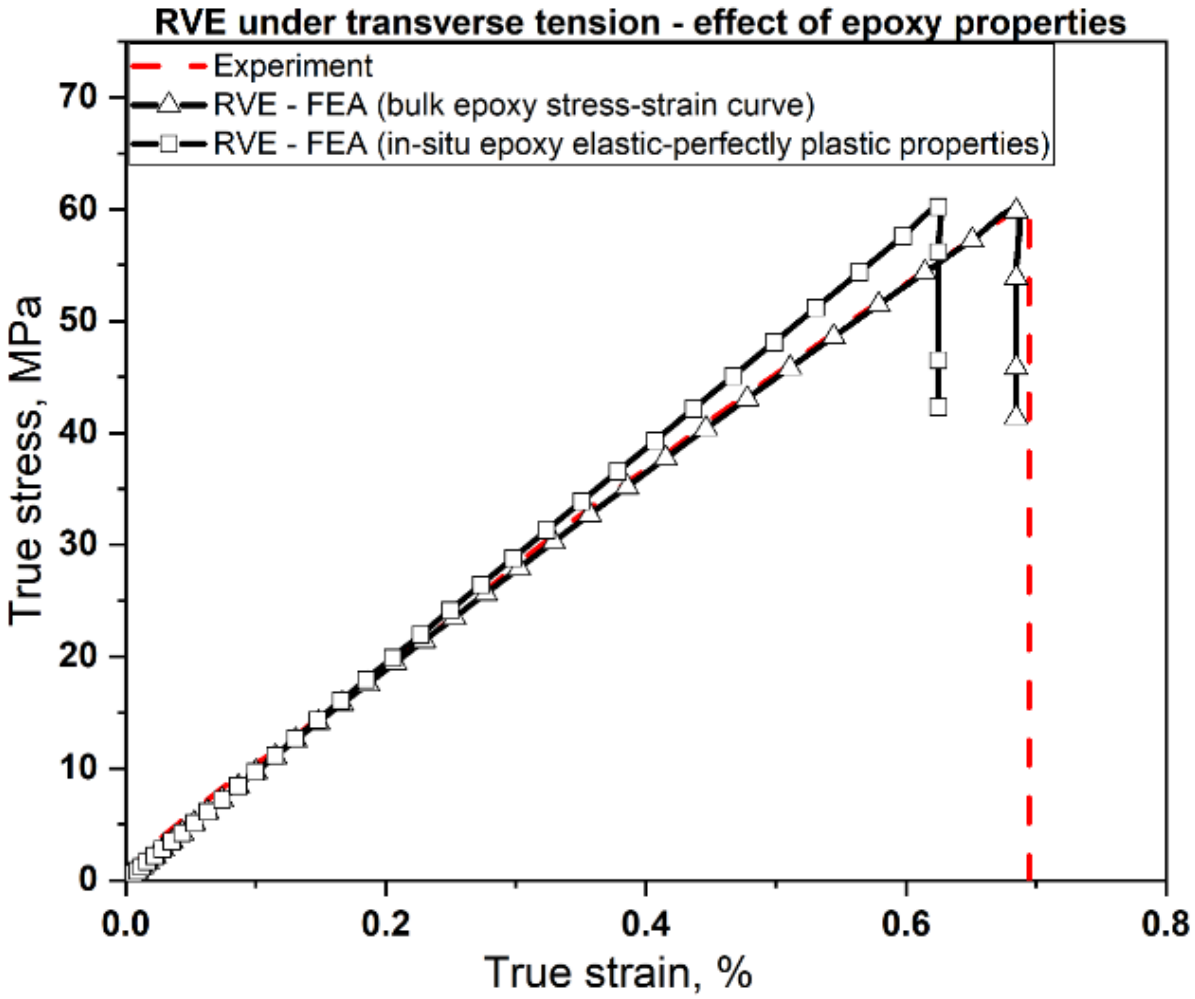

Fig 8. RVE under transverse tension: comparison between the average stress-strain curves obtained using bulk vs. in-situ epoxy material properties.

a)

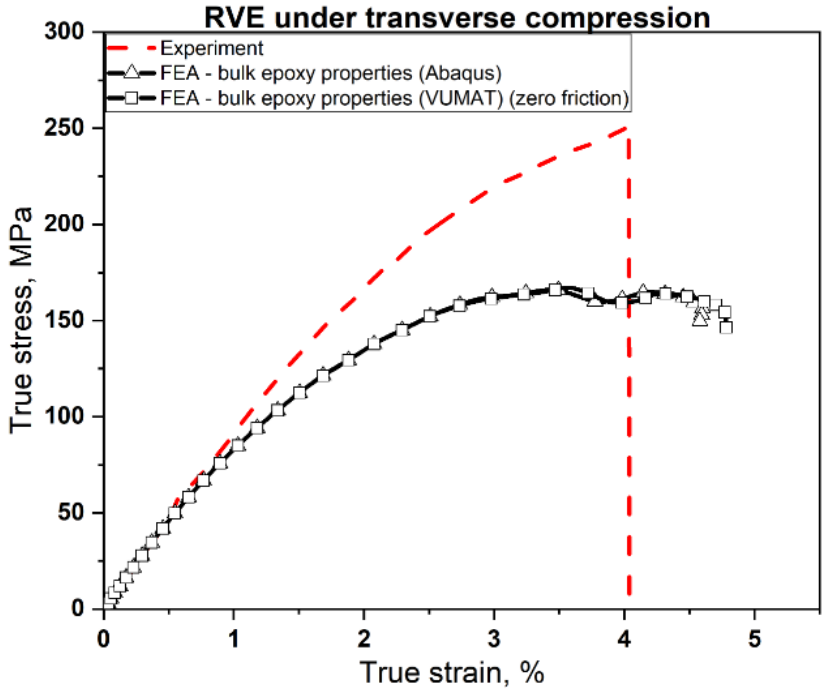
RVE under transverse compression
Experiment
FEA - bulk epoxy properties (Abaqus)
FEA - bulk epoxy properties (VUMAT) (zero friction)
True stress, MPa
True strain, %
0
50
100
150
200
250
300
0
1
2
3
4
5

b)

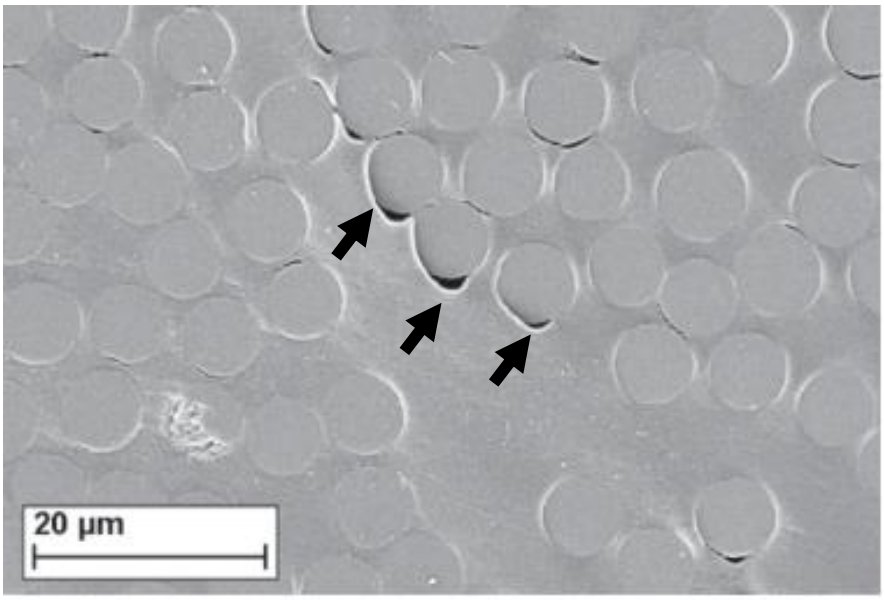
20 µm

c)

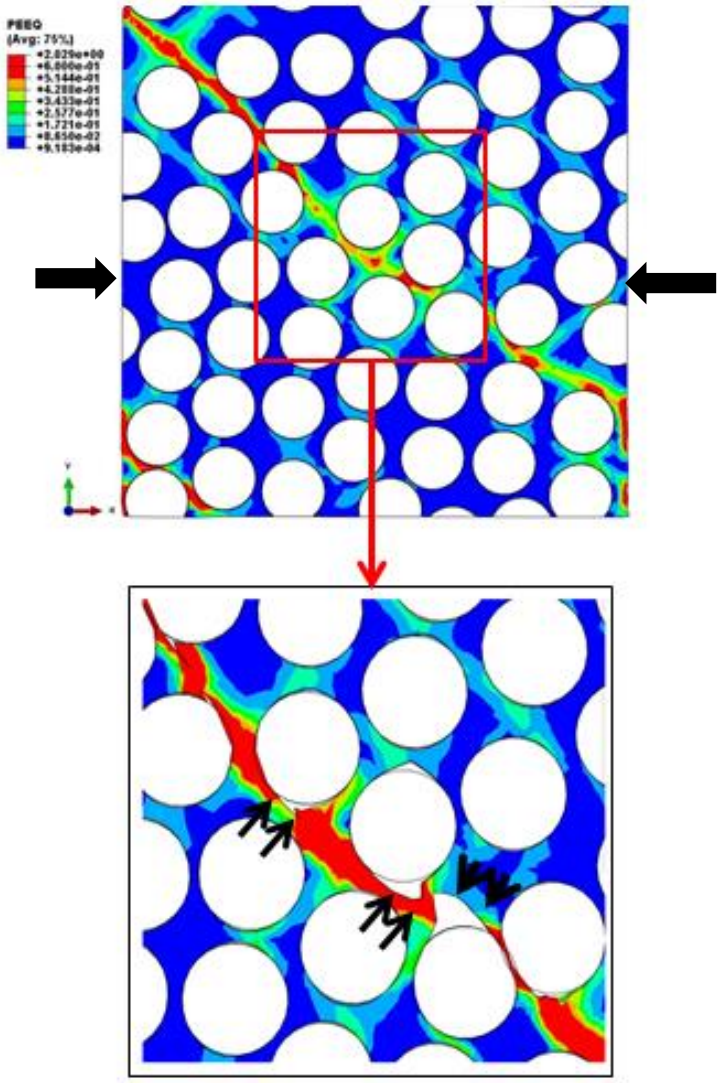

Fig 9. RVE under transverse compression: a) comparison between experimental [55] and numerical stress-strain curves; b) experimental plastic shear strain localization observed in a carbon-epoxy UD composite under transverse compression [42]; c) plastic shear strain localization observed from the micromechanical analysis.

a)

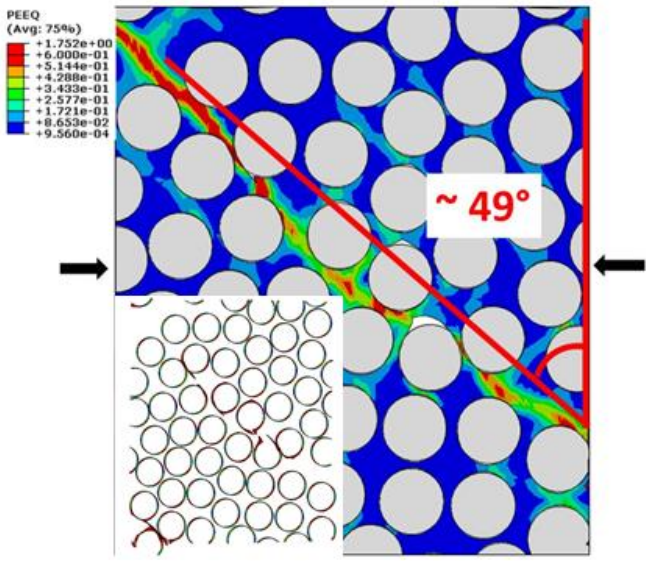

b)

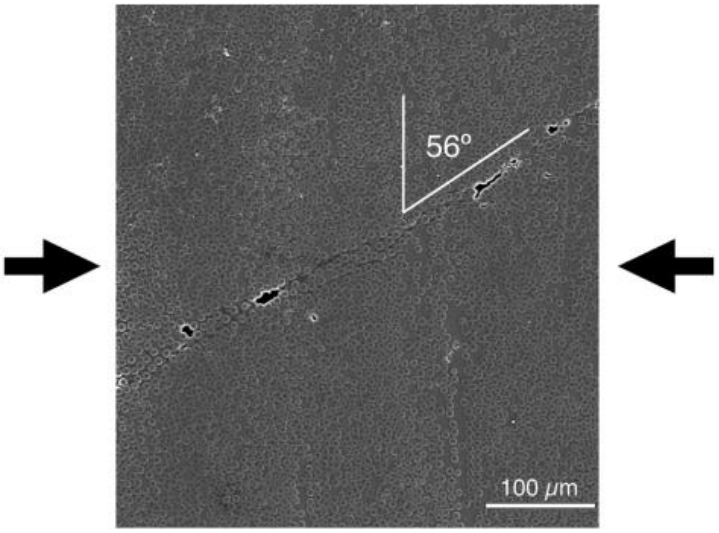

Fig 10. RVE under transverse compression: a) comparison between experimental [55] and numerical stress-strain curves; b) shear band formation in 49 fibers RVE; c) experimental plastic shear band obtained in a carbon-epoxy UD composite under transverse compression [24].

a)

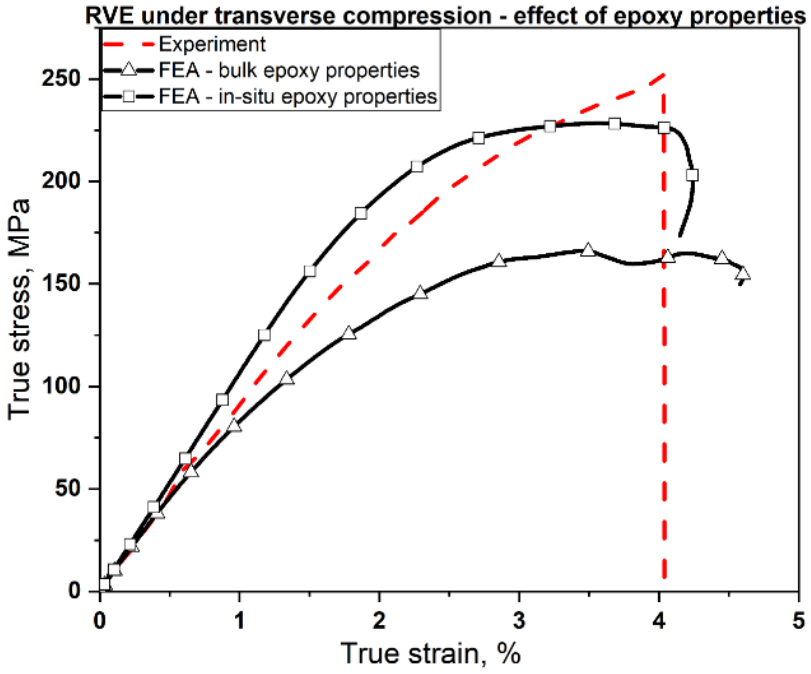
RVE under transverse compression - effect of epoxy properties
Experiment
FEA - bulk epoxy properties
FEA - in-situ epoxy properties
True stress, MPa
True strain, %
0
50
100
150
200
250
0
1
2
3
4
5

b)

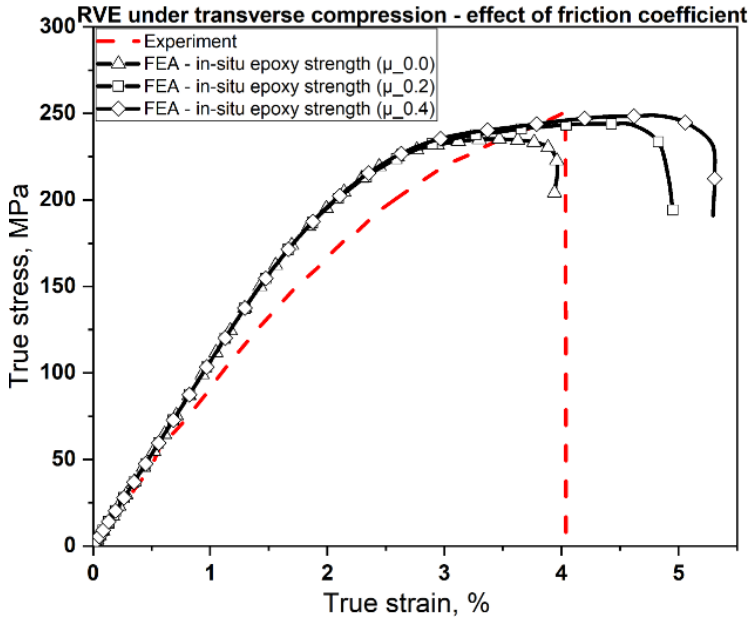
RVE under transverse compression - effect of friction coefficient
Experiment
FEA - in-situ epoxy strength (μ_0.0)
FEA - in-situ epoxy strength (μ_0.2)
FEA - in-situ epoxy strength (μ_0.4)
True stress, MPa
True strain, %
0
50
100
150
200
250
300
0
1
2
3
4
5

c)

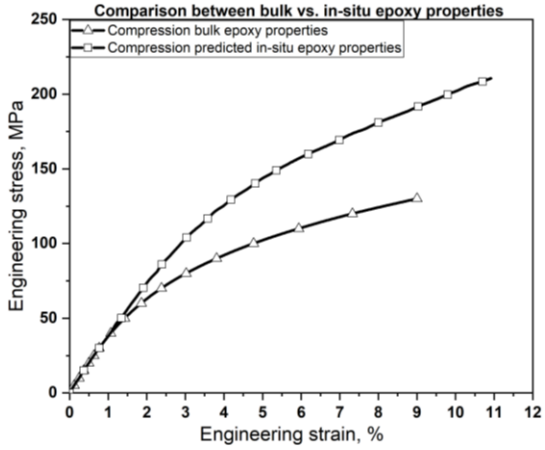

d)

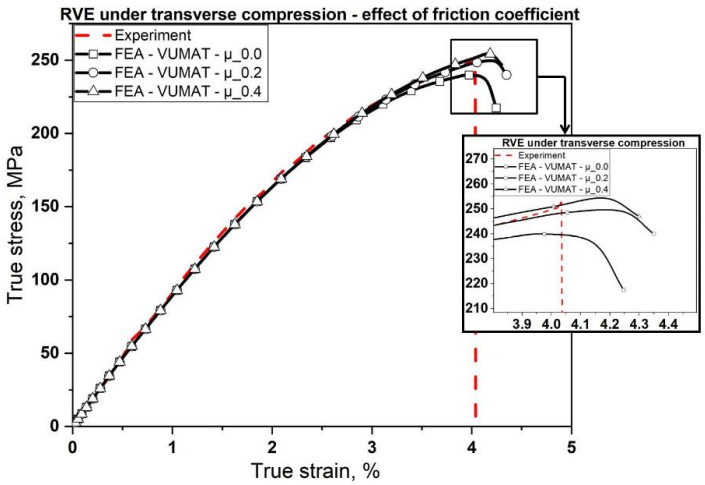

Fig 11. Effect of matrix material properties on the transverse compressive stress-strain behavior: a) predicted transverse compressive strength of the RVE using bulk and in-situ epoxy properties; b)effect of the in-situ epoxy strength and friction coefficient on the predicted compression strength; c) comparison between the predicted in-situ epoxy stress-strain curve vs. bulk epoxy stress-strain curve [49]; d) predicted transverse compressive stress-strain behavior of the RVE with the estimated in-situ epoxy non-linear stress-strain curve..

a)

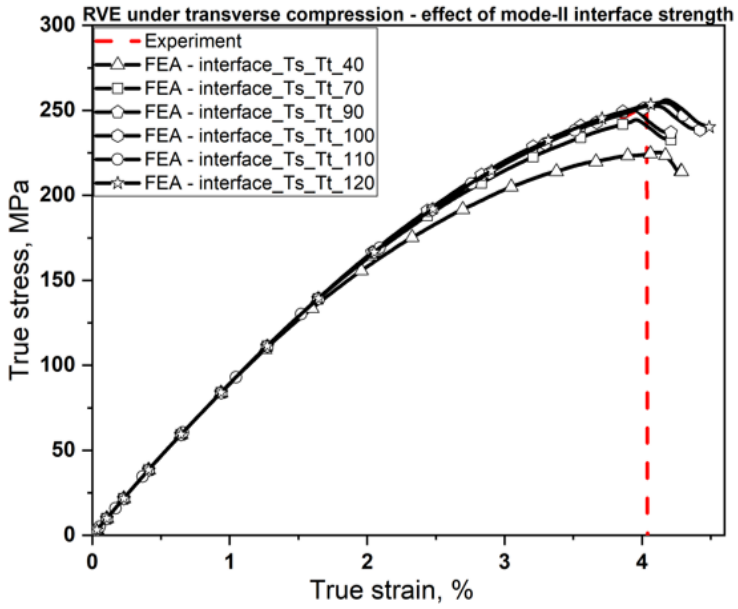

b)

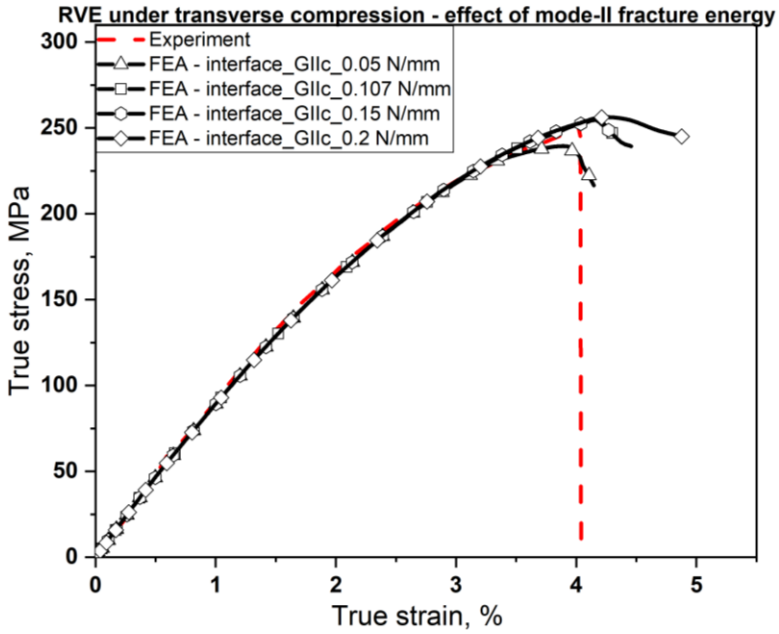

Fig 12. Effect of mode II interface properties on the transverse compression stress-strain response of an RVE: a) effect of interface strength; b) effect of interface fracture energy.

a)

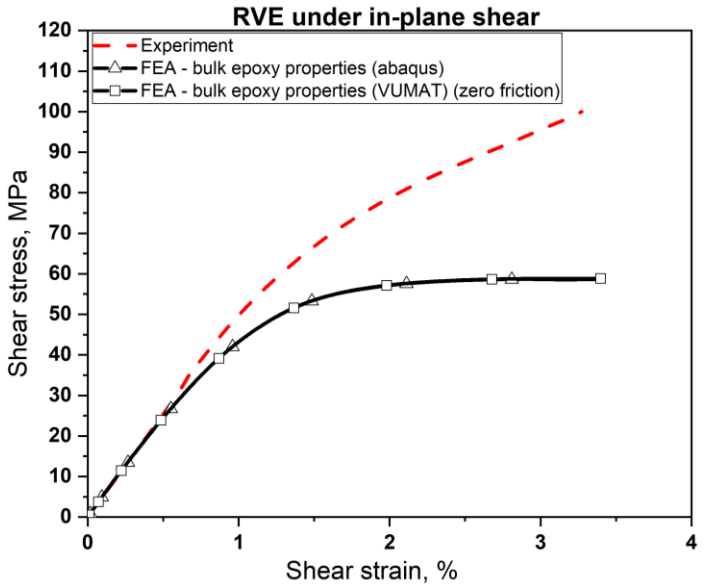
RVE under in-plane shear
Experiment
FEA - bulk epoxy properties (abaqus)
FEA - bulk epoxy properties (VUMAT) (zero friction)
Shear stress, MPa
Shear strain, %
0
10
20
30
40
50
60
70
80
90
100
110
120
0
1
2
3
4

b)

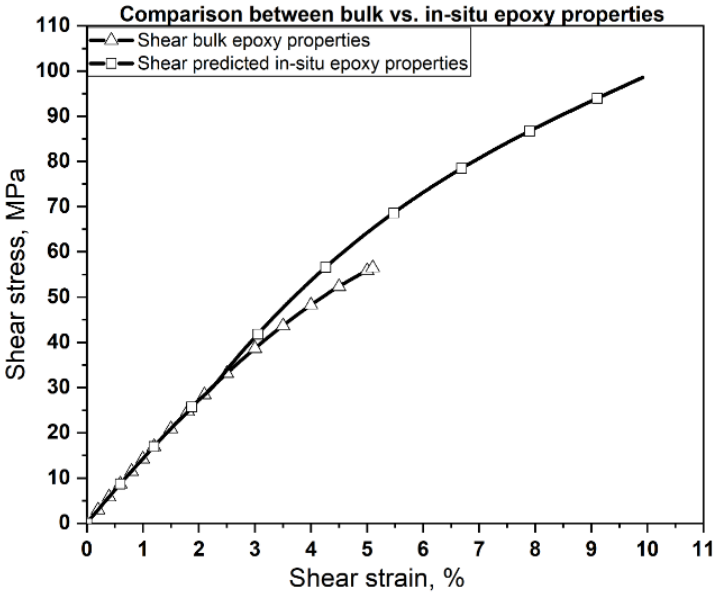
Comparison between bulk vs. in-situ epoxy properties
Shear bulk epoxy properties
Shear predicted in-situ epoxy properties
Shear stress, MPa
Shear strain, %
0
10
20
30
40
50
60
70
80
90
100
110
0
1
2
3
4
5
6
7
8
9
10
11

c)

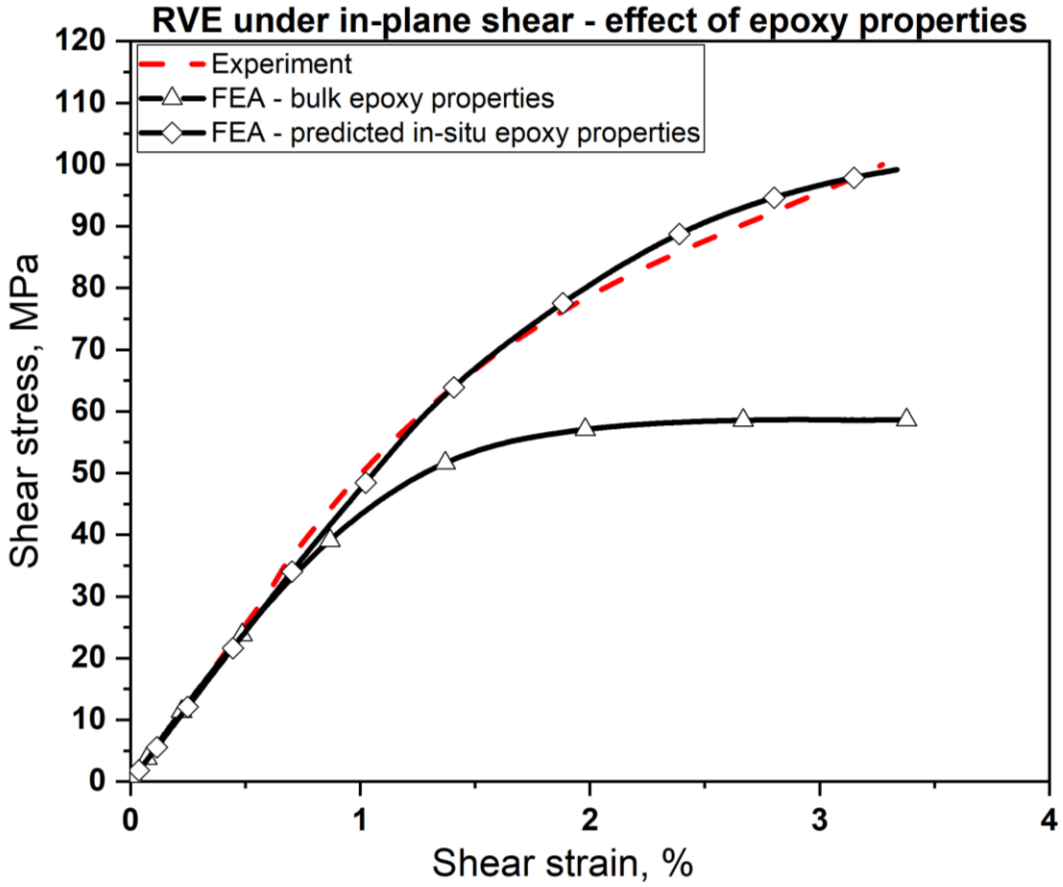

Fig 12. RVE under in-plane shear: a) comparison between experimental [50] vs. numerical prediction composite stress-strain curve using bulk epoxy properties; b) bulk vs. in-situ predicted matrix in-plane shear stress-strain curve; c) experimental [50] and predicted in-plane shear response of composite using in-situ matrix stress-strain curve.

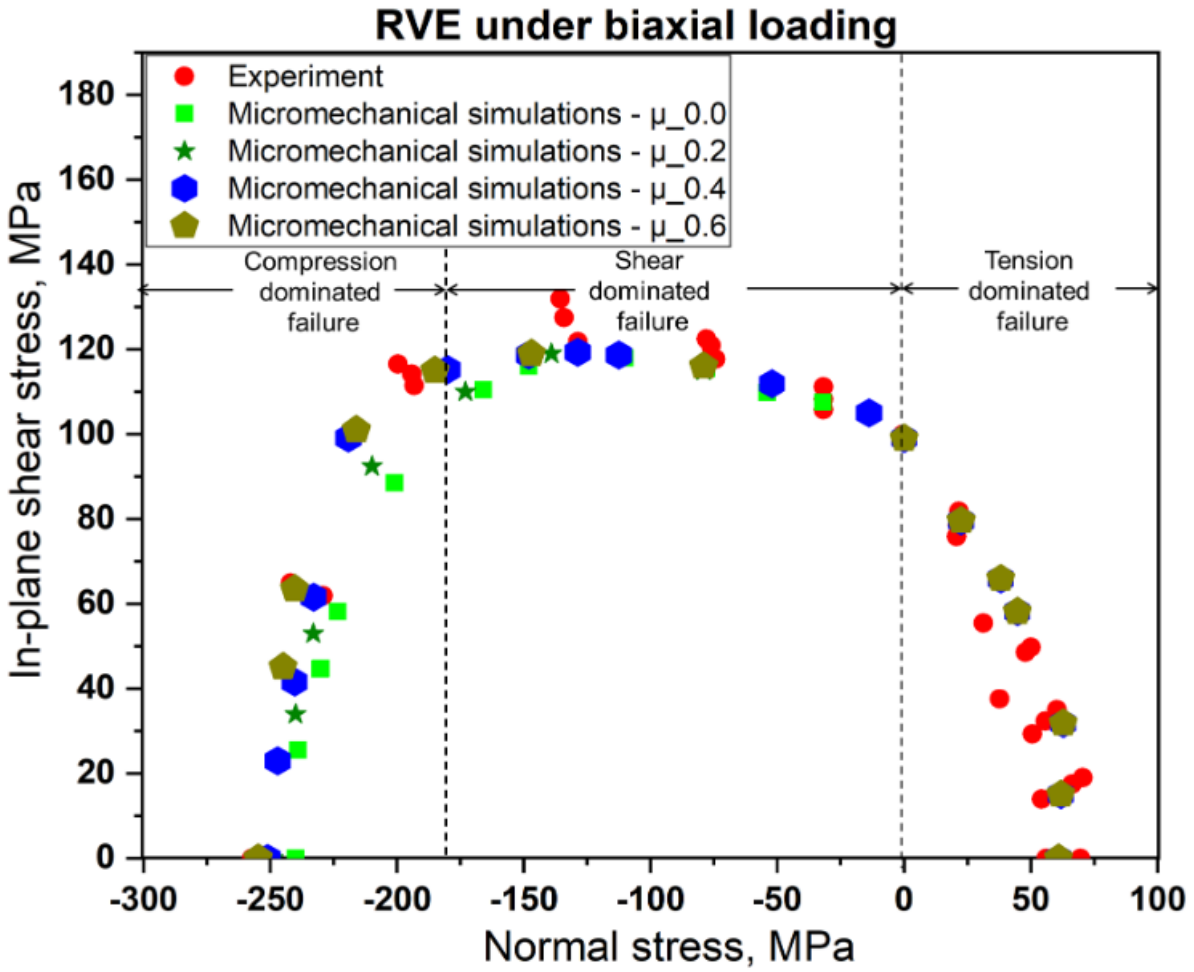

Fig 14. Comparison between the experimental [33] vs. predicted biaxial failure envelope in σ_{22}-τ_{12} stress plane with varying fiber-matrix interface friction.

a)

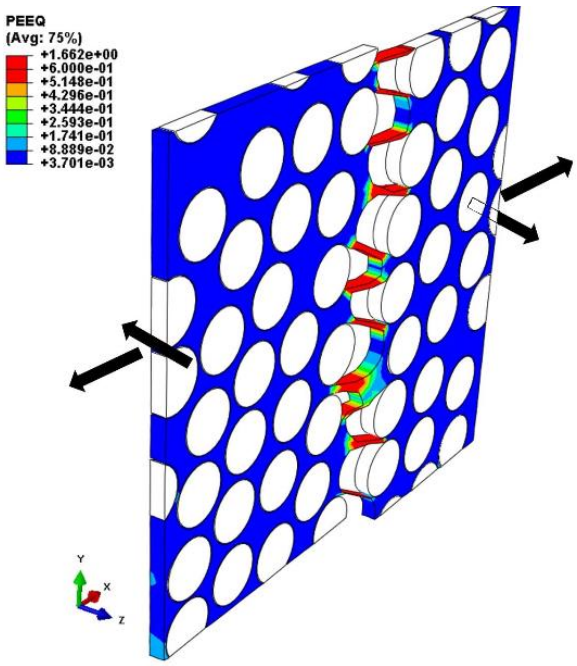

b)

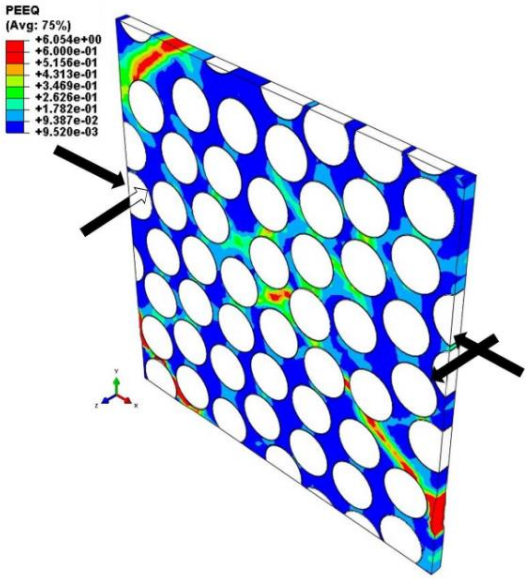

Fig 15. Failure images under combined loading: a) RVE failure image under combined transverse tension-in-plane shear load; b) RVE failure image under transverse compression-in-plane shear loading.